

# TRACKING NETWORK DYNAMICS: A REVIEW OF DISTANCES AND SIMILARITY METRICS

BY CLAIRE DONNAT AND SUSAN HOLMES

*Department of Statistics, Stanford University<sup>†</sup>*

From longitudinal biomedical studies to social networks, graphs have emerged as a powerful framework for describing evolving interactions between agents in complex systems. In such studies, the data typically consists of a set of graphs representing a system's state at different points in time or space. The analysis of the system's dynamics depends on the selection of the appropriate analytical tools. In particular, after specifying properties characterizing similarities between states, a critical step lies in the choice of a distance between graphs capable of reflecting such similarities. While the literature offers a number of distances that one could a priori choose from, their properties have been little investigated and no guidelines regarding the choice of such a distance have yet been provided. However, these distances' sensitivity to perturbations in the network's structure and their ability to identify important changes are crucial to the analysis, making the selection of an adequate metric a decisive – yet delicate – practical matter.

In the spirit of Goldenberg, Zheng and Fienberg's seminal 2009 review [11], the purpose of this article is to provide an overview of commonly-used graph distances and an explicit characterization of the structural changes that they are best able to capture. To see how this translates in real-life situations, we use as a guiding thread to our discussion the application of these distances to the analysis a longitudinal microbiome study – as well as on synthetic examples. Having unveiled some of traditional distances' shortcomings, we also suggest alternative similarity metrics and highlight their relative advantages in specific analysis scenarios. Above all, we provide some guidance for choosing one distance over another in certain types of applications. Finally, extending the scope of our analysis from longitudinal to spatial studies, we show an application of these different distances to a network created from worldwide recipes.

## CONTENTS

1	Introduction and Motivation . . . . .	2
1.1	Guiding-thread example: a Microbiome data study . . . . .	2
1.2	Problem statement and notations . . . . .	4

---

<sup>\*</sup>Supported by NIH AI112401 and NSF DMS 1501767

*MSC 2010 subject classifications:* Temporal networks; longitudinal analysis; graph distances; graph signal processing; wavelets; Microbiome; longitudinal analysis;

2	Quantifying local changes via structural distances . . . . .	7
2.1	The Hamming distance . . . . .	7
2.2	The Jaccard distance . . . . .	11
2.3	Shortcomings of local approaches . . . . .	13
3	Comparing graph structures: a spectral approach . . . . .	15
3.1	$\ell_p$ distances on the eigenvalues . . . . .	16
3.2	Spanning Tree Similarities . . . . .	18
3.3	Distances based on the eigenspectrum distributions . . . . .	21
3.3.1	General framework . . . . .	21
3.3.2	Definition of the IM distance . . . . .	21
3.3.3	The Hamming-Ipsen-Mikhailov distance . . . . .	23
3.4	The Polynomial Approach . . . . .	24
4	Quantifying change at the mesoscale . . . . .	26
4.1	Quantifying interactions: connectivity-based distances . . . . .	26
4.2	Heat spectral wavelets . . . . .	28
4.3	Application to the Microbiome study . . . . .	30
5	Case study for spatial dynamics: worldwide recipe networks . . . . .	30
6	Conclusion . . . . .	39
	References . . . . .	41
	. . . . .	41
	Appendices . . . . .	43
A	Synthetic experiments: a comparison of the different distances . . . . .	43
A.1	Structural vs Spectral distances . . . . .	44
A.2	Comparing topological signatures for heat-wavelet distances . . . . .	49
A.3	Mesoscale distances vs “Standard distances” . . . . .	56
B	Additional distance characteristics and comparisons . . . . .	58
B.1	Ipsen-Mikhailov distance . . . . .	58
B.2	Comparison with other spectral distances . . . . .	60
B.3	Heat Wavelet characteristics . . . . .	62

## 1. Introduction and Motivation.

### 1.1. Guiding-thread example: a Microbiome data study.

**Motivation.** From social sciences to biology, scientific communities across a wide number of disciplines have become increasingly interested in the study of networks – that is, graphs in which each entity or data point is assigned to a node, and existing interactions between entities are modeled by edges. If

graphs provide a versatile framework for encapsulating structural information in datasets, they also come as an indispensable paradigm in a number of applications where the study of each individual node is either irrelevant or intractable. In these cases, one is more interested in the study of the system as a whole rather than at an atomic level. Typical examples include brain connectomes, which represent brain activity by modeling neurons’ activation patterns from a network perspective (rather than by recording each individual neuron’s activity). Similarly, in microbial ecology, interactions between bacteria can be represented by a co-occurrence graph where the edges are a (carefully-selected) function of bacteria’s co-abundances. The representation of biological samples as graphs provides a richer, more informative framework than the bacterial counts themselves by highlighting co-occurrence of different bacteria. We can then associate “significant” bacterial communities to various medical conditions, such as obesity [37, 36, 15] or preterm birth [7].

**A guiding-thread example.**

We illustrate this review by using a specific microbiome study – the 2011 Relman antibiotics dataset – as our guiding thread. This longitudinal study consists of a set of 162 bacterial samples taken from the gut of three distinct subjects (D, E, and F) at different points in time, with roughly the same number of samples per subject. The subjects were given two courses of antibiotics, yielding seven distinct treatment phases (pre-treatment, first antibiotic course, week after stopping treatment 1, interim, second course of antibiotics, week after stopping treatment 2, and post-treatment phase). The goal of the study was to assess the antibiotics’ effects on microbial communities, which we analyze through two sets of graphs:

1. **bacterial symbiosis graphs:** for each subject at a given treatment phase, we define a graph in which each node corresponds to a specific bacteria, and edges  $\mathcal{E} = \{(i, j)\}$  capture pairwise “affinities” between bacteria  $i$  and  $j$ . The goal of this representation is to capture symbiotic mechanisms between bacteria: do they thrive simultaneously together – or, on the contrary – does one bacteria tend to smother the development of another? Due to the large number of zeros in the data, we define edges based on the symmetric Gini correlation [30] between bacterial counts. The symmetric Gini correlation is a non-parametric correlation measure which has been suggested as a metric for comparing relations in zero-inflated count data and which is thus appropriate for the study of microbiome co-abundances networks [27, 38].
2. **sample graphs:** we also analyze the data from a dual perspective, modeling samples as nodes and pairwise similarities between samples as edges for each of the treatment phases. The purpose of this dual

analysis is to assess the effect of the antibiotics on samples' relative distances: while initial pretreatment samples are expected to be highly variable and subject-specific – a known property of microbiome data –, a reasonable scenario is to expect the stress caused by the antibiotics to induce a convergence of the samples across subjects to a common state. To study the existence of such an effect while limiting the noisiness of our data, we divide the samples for each given treatment phase and subject into three bins – each bin corresponding to a number of consecutive samples – and compute the associated mean relative abundances. Each treatment phase is then represented by a graph on 9 nodes ( three consecutive "average gut states" within the given phase for each of our three subject). In this setting, the edge lengths are the Jaccard distances between the average samples. The Jaccard distance is a well-known metric for comparing ecological communities at different sites [9]. A few representative graphs are displayed in Figure 2.

The crux of the analysis lies in the choice of a distance capable of identifying similar "graph-states". While the thousands of taxa that constitute the human microbiome allow for a rich variety of potentially different microbial communities, these communities usually involve a very small proportion of the available taxa. In this particular analysis for instance, only 17% of the observations are non-zero.

The noise and sparsity associated to this data is illustrative of a large number of real-life applications, giving the temporal dimension of the analysis a significant importance. Indeed, not only does the signal contained in the system's dynamics complement the information provided by its point-wise study, it also plays a crucial role in ensuring the analysis' robustness to perturbation by regularizing the data. Another fundamental requirement of the analysis lies in its ability to correctly smooth the data over time while being able to capture important changes.

### 1.2. *Problem statement and notations.*

**Problem statement.** In this perspective, the definition of a distance between aligned graphs –that is, graphs encoding different instances of similarities or interactions between the same set of identified nodes– takes on a significant importance. Let us begin by emphasizing that this task is different to the classical problem of assessing the distance between two unlabeled graphs. Indeed, since the nodes have been endowed with a particular identity, there is no need to consider permutation-invariant distances. On the contrary, one

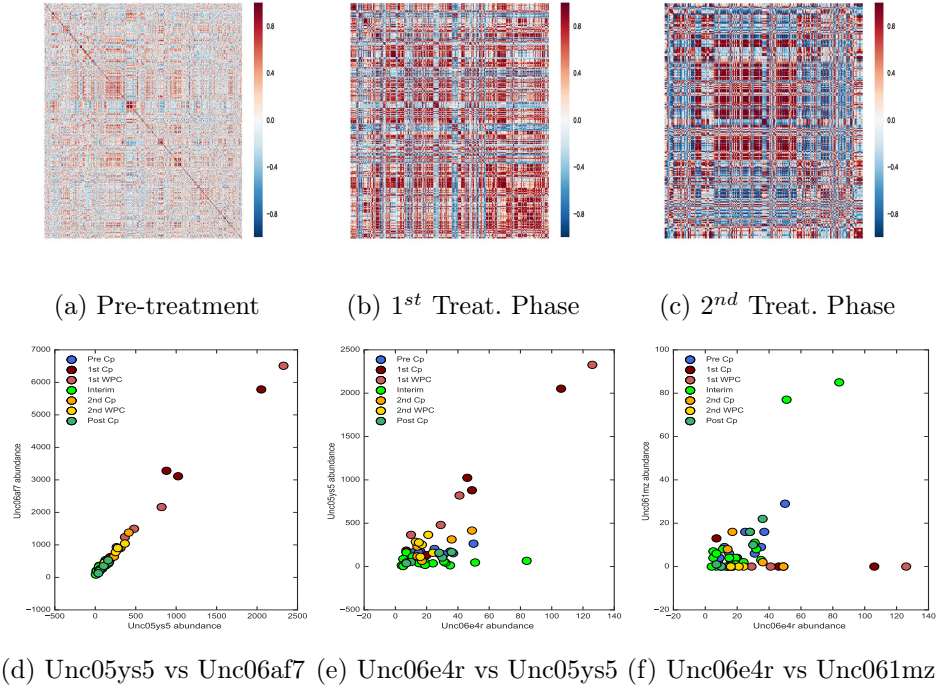
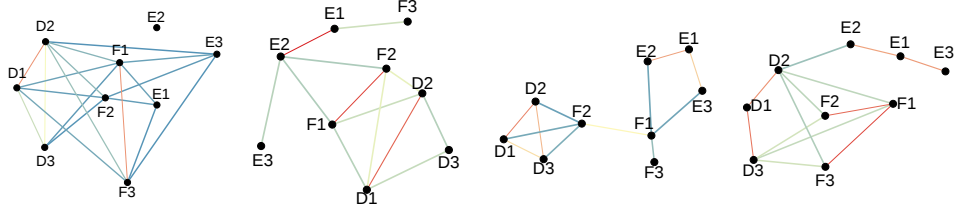


Fig 1: **Subject F. Top row:** Gini correlation between taxa abundances (rows and columns correspond to different bacteria). It is apparent from the heat maps that different treatment phases are associated with different dynamics between bacteria. **Bottom row:** Examples of bacteria pairwise relative abundances. Colors denote different treatment phases. The affinities between bacterias' dynamics vary across treatment phases.

might even wish to leverage the information contained in the nodes' labeling to define a distance sensitive to the intensity of changes at key-node locations. However, while the literature provides us with a number of "off-the-shelf" graph distances – any of which being, in principle, suited for the task –, these distances exhibit in fact distinct properties and capture different types of structural changes. For example, assessing the amount of overall network changes typically calls for a different distance than if changes are weighted by their degree of importance or impact on the structure (edges addition in sparse areas of the graph yield less redundancies and can be considered as more crucial than in densely connected areas for instance). A precise understanding of these nuances is thus mandatory to guide the selection of the most appropriate distance given the analyst's desiderata.



(a) Dual graph between samples for the Pre-treatment phase (b) Dual graph between samples for the first treatment phase (c) Dual graph between samples for the Interim phase (d) Dual graph between samples for the Post treatment phase

Fig 2: Evolution of the dual graphs across treatment phase (edges thresholded for distance superior to 0.8). Colors denote proximity of the samples' bacterial communities (*Red*: High Jaccard similarity. *Blue*: distant).

This review investigates the properties of some of the many different distances and similarities between graphs. We will include pseudo-distances – that is, metrics such that  $d(G_1, G_2) = 0$  does not necessarily imply that graphs  $G_1$  and  $G_2$  are strictly the same, but rather that they share identical “key” characteristics. Starting with structural and spectral distances – which constitute the main bulk of metrics proposed in the literature –, we highlight the dynamics and types of structural changes that these two main categories are best able to capture. An improved understanding of these metrics' properties will then allow us to suggest new similarities tailored to specific scenarios and address some of the mainstream distances' shortcomings. We introduce a new set of graph similarities based on spectral heat kernels, and argue that these similarities are optimal in that they combine both local and global structural information. In each case, the performance of the different distances is assessed on both the real microbiome dataset and synthetic, controlled experiments. Finally, we extend our illustration by applying them to the analysis of a “recipe” networks.

**Notation.** Throughout this review, we write  $G = (\mathcal{V}, \mathcal{E})$  the graph with vertices  $\mathcal{V}$  and  $\mathcal{E}$  edges. We denote as  $N = |\mathcal{V}|$  the number of nodes, and we write  $i \sim j$  if nodes  $i$  and  $j$  are neighbors. Our framework considers undirected binary graphs, with no self loops (which we extend to the study of weighted graphs in our applications).  $A$  refers to the adjacency matrix of

the graph, and  $D$  to its degree matrix:

$$A_{ij} = \begin{cases} 1 & \text{if } i \sim j \\ 0 & \text{otherwise} \end{cases} \quad \text{and} \quad D = \text{Diag}(d_i)_{i=1\dots N} \quad \text{s.t.} \quad d_i = \sum_{j=1}^N A_{ij}$$

In our case of undirected graphs, the matrix  $A$  is symmetric:  $A^T = A$ . Following standard graph theory [3], the Laplacian of the graph is the matrix defined as:  $L = D - A$ . The Laplacian is symmetric, and we consistently write its (real-valued) eigenvalue decomposition as:  $L = U\Lambda U^T$ , where  $U$  is a unitary matrix, and  $\Lambda = \text{Diag}(\lambda_i)$  is the diagonal matrix of the eigenvalues:  $0 = \lambda_0 \leq \lambda_1 \leq \dots \leq \lambda_{N-1}$ .

## 2. Quantifying local changes via structural distances.

Distances between graphs usually fall in one of two general categories, often considered as mutually exclusive: structural vs. spectral distances. The first one captures local changes, whereas the second one assesses the smoothness of the evolution of the overall graph structure by tracking changes in the eigenvalues of the graph Laplacian or its adjacency matrix. We begin by reviewing properties of standard distances falling into either one of these categories – and suggest new alternative network similarities consistent with this classification to address some of their shortcomings.

### 2.1. The Hamming distance.

**Definition.** The Hamming distance – a special instance of the broader class of Graph-Edit distances – measures the number of edge deletions and insertions necessary to transform one graph into another. More formally, let  $G$  and  $\tilde{G}$  be two graphs on  $N$  nodes, as well as  $A$  and  $\tilde{A}$  their corresponding adjacency matrices, the (normalized) Hamming distance is defined as :

$$(2.1) \quad d_H(G, \tilde{G}) = \sum_{i,j} \frac{|A_{ij} - \tilde{A}_{ij}|}{N(N-1)} = \frac{1}{N(N-1)} \|A - \tilde{A}\|_{1,1}$$

This defines a metric between graphs, since it is a scaled version of the  $L_{1,1}$  norm between the adjacency matrices  $A$  and  $\tilde{A}$ . As such, Eq. 2.1 defines a distance bounded between 0 and 1 over all graphs of size  $N$ .

**Application.** Figure 3 illustrates the results of the analysis of the microbiome study using the Hamming distance on both the bacterial (top row) and sample graphs (bottom row). We quickly remind the reader that in both cases,

the data consists in a set of graphs for each treatment phase— representing respectively symbiotic bacterial dynamics for each subject and similarities between gut bacterial communities across subjects. We here propose to use network distances to compare these graphs and focus on the analysis of: (a) the graphs’ variability from time frame to time frame, illustrated by plots of distances between consecutive graphs (figures 3B,3E) and (b) similarities across subjects or across treatment phases, illustrated by both heat maps of the pairwise distances between graphs (figures 3A,3D) and their multidimensional scaling (MDS) projections on the first two principal components (figures 3C,3F). In the bacterial case (top row), the Hamming distance exposes the existence of similar dynamics across subjects, as highlighted by the closely matching shapes of the curves (figure 3B) representing the evolution of the distances between consecutive graphs. The MDS projection (figure 3C) on the first components highlights the existence of a “treatment gradient”: interim phases –located in the top right corner of the figure– are closer to the pre-treatment samples and far from the treatment phases (violet and black points at bottom center-left of the figure). The data points corresponding to the intermediate “week after treatment 1/2” phases act as buffer between the antibiotic-independent and antibiotic-affected phases, consistent with biological interpretation of the treatment effects. While the Hamming distance does not highlight the existence of stronger similarities between samples belonging to the same individual (no darker blue blocks along the diagonal of the heat map in figure 3A), it is able to identify similar dynamic regimes across subjects – as highlighted by the clustered MDS projections of points corresponding to the same treatment phase. When applied to the dual ‘sample’ approach, the dwindling Hamming distances between consecutive sample graphs (figure 3E) shows a drastic difference in the way that treatment 1 and 2 affect the sample graphs: the first treatment phase is characterized by a radically different structure than the pre-treatment sample graph, whereas this difference subsides for the second treatment . It also shows a high proximity of the interim graph to the pre and post-treatment graphs (blue patches in figure 3D), consistent with the fact that these phases are dominated by a high “subject effect” (the gut microbiome in these phases being highly variable from individual to individual). Similarly, the graphs during treatment phases (1<sup>st</sup> CP and 2<sup>nd</sup> CP) are closer to each other than to any other sample graphs. On the other hand, the sample graphs in the first treatment course and the week after this treatment has stopped (1<sup>st</sup> CP vs 1<sup>st</sup> WCP) are identified as the most dissimilar ones in the dataset, highlighting the fact that the antibiotics modifies the original “subject-clustered” structure of the sample graphs.



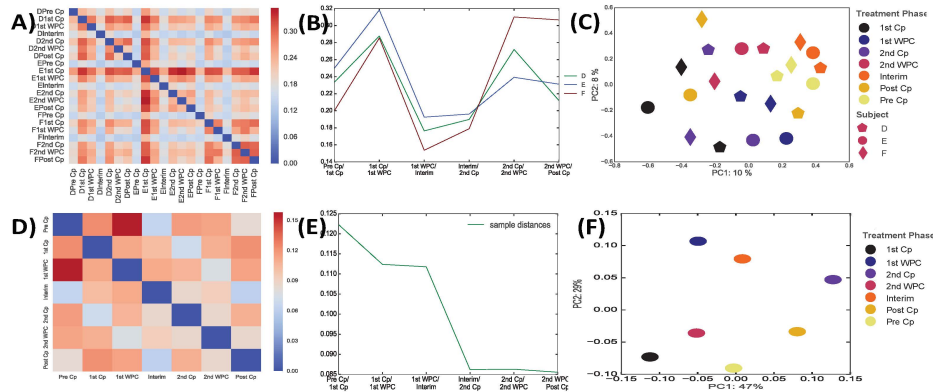


Fig 3: Application to the Microbiome study: Hamming distance between bacterial graphs (top row), and sample graphs (bottom row, as in 2). Heatmap of the Hamming distances between Gini-correlation-based bacterial graphs (A) and dual sample graphs (D). Plots of the consecutive distances between bacterial graphs (B) and dual sample graphs (E). MDS projection of the bacterial (C) and sample (F) graphs on the first two principal axes. Colors denote treatment phases, and shapes represent different subjects.

**Discussion.** With a cost complexity of the order of  $O(N^2)$ , the Hamming distance provides a straightforward way of comparing sequences of aligned graphs that only takes into account the number of shared edges. It thus comes as no surprise that this distance appears as a long-time favorite in various graph comparison problems. Graph embedding techniques – which consist in trying to find a vector-valued representation for each graph capturing its geometric properties – are a case in point: in [26], the authors define similarities between subgraphs through their graph-edit distance. Similarly, in [10], the authors introduce the notion of a “median graph” as the minimizer of the sum of pairwise graph-edit distances.

While the Hamming distance is a perfectly valid first candidate graph distance for any type of analysis, it is worth emphasizing that it only reveals some restricted aspect of network similarities.

The first trait to highlight is its uniform treatment of all changes in the graph structure: all additions and deletions are assumed to have similar importance. In particular, changes in the network’s core are treated equivalently to changes in the periphery. We will analyze the consequences and limitations of this assumption in section 2.1.3. A second trait is Hamming’s sensitivity to

the density of the graphs. This has two consequences: (a) a limited capacity to recognize similar dynamical processes across graphs with varying sparsity and (b) a potential under-estimation of distances when one graph is a super set of the other. As an example of the first point, let us consider a dynamic regime in which, at every time point, each edge is randomly flipped independently of the others: it either stays in the graph or disappears with probability  $p$ . The total number of disappearances follows a binomial distribution with mean  $p|\mathcal{E}|$ . For an identical perturbation mechanism, dense graphs are thus placed at higher distances to each other – and are thus considered as more unstable – than sparse graphs. The Hamming distance is unable to recognize that these graphs share in fact the same level of relative variability, which can hinder some aspects of the analysis. Indeed, the random deletion process at hand can be thought of as “blurring noise” applied to a “true” underlying graph structure, and is a typical model to represent our inability to observe all interactions between nodes in a complex system. In this case, it seems more natural to specify the inherent variability of the data in terms of “noise level” rather than “noise quantity”, and our analysis should thus recognize similar noise levels independently of the graphs’ original sparsity. Similarly, the Hamming distance tends to place nested graphs at a smaller distance to each other than other metrics. Indeed, suppose that graph  $\tilde{G}$  comprises 50% of the edges of graph  $G$ . The Hamming distance between the two graphs is then simply  $d(G, \tilde{G}) = \frac{0.5|A|}{N(N-1)}$ , and does not correct for the size of the initial graph. We could nonetheless argue that this distance should be big (or at least close to 0.5), since the structure of the system is radically modified. Our microbiome study is a case in point (Fig. 3B): the variety of the microbiota involved in the interim phase jumps to almost twice its corresponding value in any of the antibiotics phases (the number of bacteria increases from around 210 bacteria to 420). The distances between the interim phase and the other phases are subsequently smaller than for any of the other phases, with a number of shared taxa.

The Hamming distance is thus a measure of the *amount of change* between two graphs. It operates under the assumptions that (1) all nodes and edges are equivalent – in other words, that the location of the perturbation is irrelevant to its importance– and (2) that similarities between graphs are only characterized by the number of shared edges. While this might be adequate for characterizing the evolution of a given system through time, it is nonetheless unfit for finding similarities in broader settings. In particular, tasks such as comparing evolution processes for graphs with different densities or recognizing instances of the same network family (Erdős-Rényi random graphs, Power-Law graphs, etc.) indubitably require other metrics.

2.2. *The Jaccard distance.*

**Definition.** A potential solution to the aforementioned density-effect problem consists in using the Jaccard distance [25], which includes a normalization with respect to the volume of the union graph:

$$(2.2) \quad d_{\text{Jaccard}}(G, \tilde{G}) = \frac{|G \cup \tilde{G}| - |G \cap \tilde{G}|}{|G \cup \tilde{G}|} = \frac{\sum_{i,j} |A_{ij} - \tilde{A}_{ij}|}{\sum_{i,j} \max(A_{ij}, \tilde{A}_{ij})} = \frac{\|A - \tilde{A}\|_{1,1}}{\|A + \tilde{A}\|_*}$$

where  $\|\cdot\|_*$  denotes the nuclear norm of a matrix.

Eq. 2.2 is known to define a proper distance between the graphs. A straightforward way to see this is to use the Steinhaus Transform, which states that for  $(X, d)$  a metric and  $c$  a fixed point, the transformation  $\delta(x, y) = \frac{2d(x,y)}{d(x,c)+d(y,c)+d(x,y)}$  produces a metric. We apply here this transformation with  $d$  the Hamming distance and  $c$  the empty graph:

$$\begin{aligned} \delta(G, \tilde{G}) &= \frac{2\|A - \tilde{A}\|_{1,1}}{\|A\|_{1,1} + \|\tilde{A}\|_{1,1} + \|A - \tilde{A}\|_{1,1}} = \frac{2(|G \cup \tilde{G}| - |G \cap \tilde{G}|)}{2|G \cup \tilde{G}|} \quad (*) \\ &= d_{\text{Jaccard}}(G, \tilde{G}). \end{aligned}$$

In particular, taking for instance  $G = G_t$  and  $\tilde{G} = G_{t+1}$  the graphs associated to the state of a system at two consecutive time points  $t$  and  $t+1$  (with  $\mathcal{E}_{G_t}$  and  $\mathcal{E}_{G_{t+1}}$  their respective set of undirected edges) and rewriting the left hand side of (\*), we have:

$$(2.3) \quad \begin{aligned} d_{\text{Jaccard}}(G_t, G_{t+1}) &= \frac{d_{\text{Hamming}}(G_t, G_{t+1})}{\frac{|\mathcal{E}_{G_t}| + |\mathcal{E}_{G_{t+1}}|}{2N(N-1)} + \frac{1}{2}d_{\text{Hamming}}(G_t, G_{t+1})} \\ \implies d_{\text{Jaccard}}(G_t, G_{t+1}) &= \frac{\frac{d_{\text{Hamming}}(G_t, G_{t+1})}{\bar{S}}}{1 + \frac{d_{\text{Hamming}}(G_t, G_{t+1})}{2\bar{S}}} \end{aligned}$$

with  $\bar{S} = \frac{|\mathcal{E}_{G_t}| + |\mathcal{E}_{G_{t+1}}|}{2N(N-1)}$  is the average sparsity of the two graphs.

**Application.** figure 4 shows the result of the analysis carried out using the Jaccard distance. Since the edges in our graphs have been assigned different weights according to the intensity of the interaction between bacteria, we have used the version of the Jaccard distance extended to the weighted graph

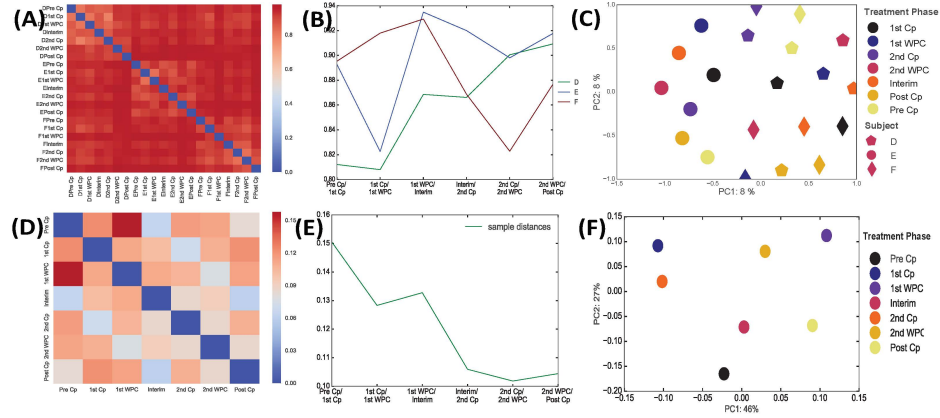


Fig 4: Application to the Microbiome study: Jaccard distance between bacterial graphs (top row), and sample graphs (bottom row, as in figure 2). Heatmap of the Jaccard distances between Gini-correlation-based bacterial graphs (A) and dual sample graphs (D). Plots of the consecutive distances between bacterial graphs (B) and dual sample graphs (E). MDS projection of the bacterial (C) and sample (F) graphs on the first two principal axes. Colors denote treatment phases, and shapes represent different subjects.

setting, defined as:

$$d_{\text{Jaccard}}(G, \tilde{G}) = 1 - \frac{\sum_{i,j} \min(A_{ij}, \tilde{A}_{ij})}{\sum_{i,j} \max(A_{ij}, \tilde{A}_{ij})}.$$

Note here that this analysis yields very different results compared to the Hamming distance. In particular, the samples are almost uniformly far from each other in both the bacterial and sample dual graphs (figures 4A,4D, 4C,4F). On the whole, there is less coherence in the subject dynamics than in the Hamming analysis: the curves in figure 4B have less closely matching shapes, and the Jaccard distance seems to mainly emphasize a dominating subject effect – as opposed to the "treatment phase" effect highlighted by the Hamming distance. Indeed, points with similar shape are generally closer to each other in figure 4C, and we note slightly lighter blocks along the diagonal in figure 4A corresponding to the subjects. Interestingly, the dual sample graphs exhibit very similar behaviors for both the Hamming and Jaccard distances.

**Discussion.** The Jaccard distance adjusts for the density by including a normalization of the Hamming distance using the average sparsity of the two graphs. As such, it reflects the *amount of change with respect to the initial*

*graph structure.* To highlight the benefits of this property, let us consider a dynamic regime in which the total number of edges stays fixed, but at each time point, each edge is replugged with probability  $p$  in a previously vacant spot: the overall number of edges remains identical, but each flipped edge induces an increase in the Hamming distance of size  $\frac{4}{N(N-1)}$ . Hence, the average Hamming distance between  $G_t$  and  $G_{t+1}$  admits a closed-form expression of the type:

$$d_{\text{Hamming}}(G_t, G_{t+1}) = \frac{4p|\mathcal{E}|}{N(N-1)} = 4ps$$

where  $s = |\mathcal{E}|/(N(N-1))$  is the sparsity of the original graph. By Eq. 2.3, the Jaccard distance can be written as:  $d_{\text{Jaccard}}(G_t, G_{t+1}) = \frac{4p}{1+2p} = 2[1 - \frac{1}{1+2p}]$ , where the later expression is a strictly increasing function of  $p$ . The Jaccard distance is thus independent of the sparsity and defines a one-to-one mapping between the rate of change  $p$  and the observed distance. In contrast, the effect of  $p$  is confounded in Hamming distance by the influence of the sparsity.

This simple example shows that the Jaccard distance is better suited to comparing different dynamics, where the rate of change is the main quantity of interest. Another of its advantages with respect to the Hamming distance is that it also provides a more interpretable notion of pairwise distances. Indeed, the Jaccard distance can be understood as the proportion of edges that have been deleted or added with respect to the total number of edges appearing in either network: a Jaccard distance close to 1 indicates an entire remodeling of the graph structure between time  $t$  and  $t+1$ . In the microbiome study at hand, the Jaccard distance reveals more variability in the bacterial than the Hamming distance: it highlights the fact that for each subject, the bacterial graph undergo drastic changes between treatment and interim/ post-treatment phases.

### 2.3. Shortcomings of local approaches.

While the Hamming and Jaccard distances provide straightforward ways of analyzing a graph’s evolution over time, such measures oftentimes appear too myopic. Indeed, these metrics focus on the direct neighborhood of each node, and fail to capture the “bigger picture” and information on the evolution of the graph as a whole. figure 5 shows an example where a network  $G_0$  undergoes two different evolution processes, yielding distinct graph structures with similar Hamming distance to the original. In this setup, it is possible to argue that  $G_1$  and  $G_2$  are more similar to each other, since the maximal path length between any two nodes is 2, whereas information percolates less

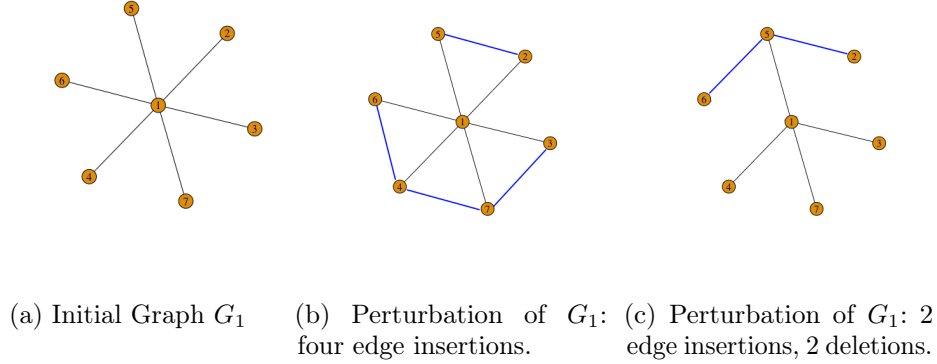


Fig 5: Two modifications of the same initial graphs (displayed in figure 5a, such that the Hamming distance with the original is  $d_H(G_1, G_2) = d_H(G_1, G_3) = \frac{4}{21}$ , and the Jaccard distances are  $d_J(G_1, G_2) = \frac{2}{5}$  and  $d_J(G_1, G_3) = \frac{1}{4}$ . The average shortest path length are 1.71 for the initial graph  $G_1$ , 1.51 for  $G_2$  and 2 for  $G_3$

rapidly across the network in the third. Conversely, from another perspective, we could also argue that we should have  $d(G_1, G_3) \leq d(G_1, G_2)$ , since the two first share a higher number of nodes with identical degree or since they have the same number of spanning trees. This example is meant to show that distances can be adapted to capture specific aspects of a network's properties. In fact, in [24], Koutra and al. propose to define a "good" similarity score between graphs as a score satisfying the following set of four characteristics:

1. **Edge-Importance:** modifications of the graph structure yielding disconnected components should be penalized more.
2. **Edge-Submodularity:** a specific change is more important in a graph with a few edges than in a denser graph on the same nodes.
3. **Weight Awareness:** the impact on the similarity measure increases with the weight of the modified edge.
4. **Focus awareness:** random changes in graphs are less important than targeted changes of the same extent.

These serve as guidelines and can be modified and enriched by the data analyst depending on the application at hand. The Jaccard and Hamming distance treat all edges uniformly, irrespective of their status (thus violating criterion 2 for instance), thus calling for the definition of alternative distances or dissimilarity score.

### 3. Comparing graph structures: a spectral approach.

As pointed out above, purely structural distances fail to capture some important information encoded in the overall structure of the network. Spectral distances, on the other hand, are global measures defined using the eigenvalues of either the adjacency matrix  $A$  or of the Laplacian  $L$ . Consistently with the notations introduced in section 1, the Laplacian of the graph is defined as:  $L = D - A$ , where  $D$  is the diagonal matrix such that  $D_{ii}$  is the degree of node  $i$ . For the sake of simplicity and interpretability of the results, we choose  $L$  to be the combinatorial Laplacian. The normalized Laplacian  $\tilde{L} = I - D^{-1/2}AD^{-1/2}$  is also a valid choice with roughly similar properties.

A first natural question behind the motivation for this approach is “why?”: why should eigenvalues better characterize the state of a graph? Let us first provide some intuition for this spectral approach. The eigenvalues of a graph characterize its topological structure, and in particular the way that energy or information localized at a particular node can be propagated over the graph. As such, they are related to the stability of the complex system that the graph represents. In quantum chemistry for instance, hydrocarbons are typically represented by graphs, whose eigenvalues correspond to energy levels of its electrons. In physics, the eigenvalues of the Laplacian represent the vibrational frequencies of the heat equation. The analysis of the spectral properties of a graph thus provide considerable insight into the dynamics of the system as a whole.

In this section, we will brush an overview of various spectral distances. Such distances have been well studied and developed in the literature [21, 17, 2]. In [20] for instance, the authors brush an interesting review of several of such spectral distances. This however deviates slightly from our original setup: spectral distances are permutation invariant and do not take into account the fact that nodes have been endowed with a particular identity. In fact, such distances can be used to compare any set of graphs, provided that they all share the same number of nodes. Spectral distances are unable to distinguish between isospectral graphs and are in fact pseudo-distances (which capture similarities between states) rather than actual distances. However, as the probability of having distinct graphs with identical eigenspectra quickly dwindles as the number of nodes increases, spectral distances are also viable candidates for studying the dynamics of a given complex system through time. While most current algorithms can compute eigenvalue decompositions in  $O(N^3)$  steps, some computational tricks bring down this cost to  $O(N^2)$  [34]—thus making this spectral approach an appealing, computationally tractable

alternative for defining graph similarities [1, 12].

### 3.1. $\ell_p$ distances on the eigenvalues.

**Definition.** We begin by introducing a general class of versatile spectral distances. A first natural candidate for comparing two graphs based on their eigenvalue decomposition is to simply consider the  $\ell_p$  distance between functions of their Laplacian’s eigenspectra. This is well suited to our “aligned-graph” setting, since we know that the graphs have the same number of nodes, and hence, the same number of eigenvalues. Moreover, eigenspectra are known to be robust to most perturbations: a “small” perturbation of the graph –that is, a perturbation that has very little impact on the graph’s overall connectivity– will only induce a small change in the eigenvalues [33].

For any monotonic, (almost everywhere) differentiable function of the Laplacian’s eigenvalues  $\lambda_0 \leq \lambda_1 \leq \dots \leq \lambda_{N-1}$ , we can write:

$$(3.1) \quad d(L, \tilde{L})^p = \sum_{i=1}^{N-1} |f(\lambda_i + \epsilon_i) - f(\lambda_i)|^p \approx \sum_{i=1}^{N-1} |f'(\lambda_i)|^p |\epsilon_i|^p$$

We note in passing that the first eigenvalue  $\lambda_0$  is always 0 – which is why the summation includes only  $N - 1$  terms.

**Application.** Let’s look at the spectral distances on our microbiome data. Figure 6 shows the results for the  $\ell_2$  distance using two functions of the eigenspectra in Eq. 3.1: the identity  $f(x) = x$  (top row) and a low-pass filter  $f(x) = \mathbb{1}_{x < 2}(x)$  (bottom row). For the purpose of simplicity, we only present the results for the bacterial graphs (eigenspectrum-based distance appear less suited to very small graphs, where perturbations of edges have typically larger effects on the connectivity of the graph). The first interesting observation that we make is that these distances produce different results, highlighting the impact of the choice of the function  $f$  for the analysis. While both distances push the analysis beyond the recognition of a subject effect by highlighting higher similarities between graphs corresponding to the same treatment phase (clustering of points with same color in Figures 6C-6F), the low-pass filter-based distance recovers in particular a cluster comprising Pre-treatment and Interim phases (Figure 6F) – thus emphasizing the fact that these phases are characterized by different dynamics than the other treatment phases. The low-filter distance also highlight how the graphs belonging to the different subjects undergo similar dynamics (as shown by the closely matching curves in Figure 6E), an aspect which is not compellingly put forward by the vanilla identity-based distance. This later distance seems to struggle to



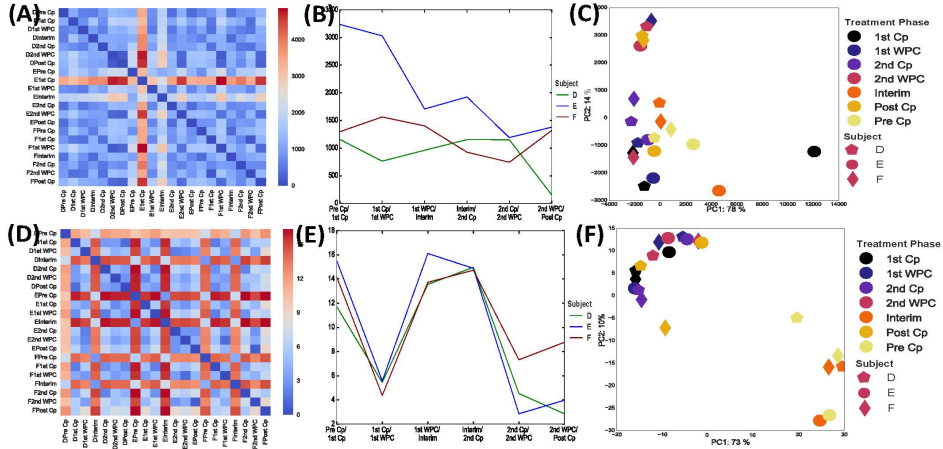


Fig 6: Application of  $\ell_2$  spectral distances using two functions of the eigenspectra in Eq. 3.1: the identity  $f(x) = x$  (**top row**) and a low-pass filter  $f(x) = \mathbb{1}_{x < 2}(x)$  (**bottom row**). Heat map of the corresponding distances between bacterial graphs (**A**) / (**D**). Plots of the consecutive distances between bacterial graphs (**B**) / (**E**). MDS projection of the bacterial (**C**) / (**F**) graphs on the first two principal axes. Colors denote treatment phases, and shapes represent different subjects.

capture similarities between graphs: all graphs seem uniformly distant to each other and this distance does not pick up on any block structure in Figure 6A. The only exception lies in the first treatment phase of subject E, which is extremely distant from all the others and thus appears to be an outlier. The fact that this difference is not picked up upon in the low-pass graph seems to indicate that the main difference of the graph with respect to the others occurs in the higher end of its eigenspectrum – an effect that can be attributed to noise as we will detail in the next paragraph.

**Discussion.** The choice of the function  $f$  depends on the type of analysis:

- If the goal of the analysis is to capture *the importance of the changes in the connectivity of the overall graph structure*, the distance should put more emphasis on the first eigenvectors. As emphasized in [31], the eigenvalues of the Laplacian can be interpreted as the analog to a signal's frequencies in the temporal domain. Low eigenvalues and their corresponding eigenvectors are analogous to slowly-varying low-frequency signals over the graph: if two vertices are connected by an edge with a large weight, the values of the eigenvector at those locations are likely to be similar. By contrast, the eigenvectors associated to high eigenvalues vary more rapidly across edges [32, 35]. Hence, "low"

eigenvectors encapsulate more information about the structure of the graph. An adequate choice for  $f$  would be thus to select  $f$  to act as a low-pass filter: putting more weight on changes occurring in small eigenvalues, and discounting the effect of changes at the higher end of the spectrum. The strength of the modulation of the eigenvalues by the filter depends on the analysis. For instance, taking  $f : x \rightarrow e^{-\alpha x/\lambda_3}$  ensures associating a weight of at most  $\frac{\alpha}{\lambda_3} e^{-\alpha}$  in Eq. 3.1 on changes in eigenvalues greater or equal to  $\lambda_3$ . In the case where  $\lambda_2 \ll \lambda_3$ , this gives more importance to changes occurring in  $\lambda_2$ . In our microbiome study, as previously highlighted, we recover more structure in the dataset by focusing on the lower part of the spectrum (Figure 6) and discarding the higher frequency, “noisier” eigenvalues.

- Supposing that one is interested in the *overall change in the “graph’s frequencies” at every level* induced by the perturbation, one might actually prefer to take a function that would not discriminate against any value of the eigenfunction, but simply look at the amplitude of the change in eigenvalue. In that case,  $f$  could simply be taken to be the identity.

This section has shown the possibility of crafting a distance based on the Laplacian eigenspectrum, tailored to the requirements and objectives of the analysis. However, choosing “an optimal” kernel function for the problem at hand requires domain knowledge or additional insight into the problem – thus requiring more thought than the straightforward Hamming distance.

### 3.2. Spanning Tree Similarities.

**Definition.** Inspired by A. Kelmans [22, 23], who characterized transformations by their “ability to destroy”, we now introduce a similarity which reflects the number of spanning trees that are destroyed or created by the transformation of one graph to another.

The Matrix-Tree theorem provides us with a convenient way of computing the number of spanning trees for a connected graph: denoting  $0 = \lambda_0 < \lambda_1 \leq \dots \leq \lambda_{N-1}$  the eigenvalues of the Graph Laplacian  $L = D - A$ , we have:

$$\mathcal{T}_G = N_{\text{Spanning tree of } G} = \frac{1}{N} \prod_{i=1}^{N-1} \lambda_i$$

A dissimilarity between two graphs  $G$  and  $\tilde{G}$  can be defined by comparing the quantities:

$$(3.2) \quad d_{ST}(G, \tilde{G}) = \left| \log(\mathcal{T}_G) - \log(\mathcal{T}_{\tilde{G}}) \right|$$

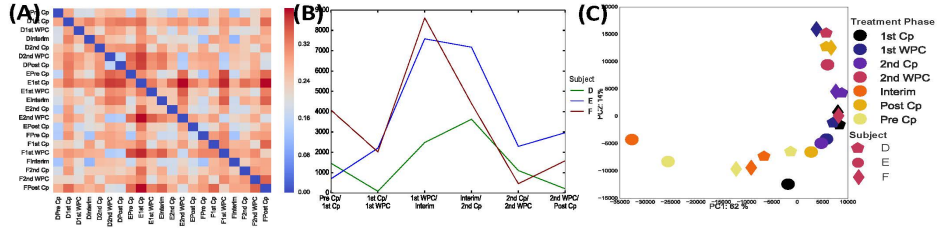


Fig 7: Application of the Spanning tree dissimilarity. Heatmap of the corresponding dissimilarity between Gini-correlation-based bacterial graphs (A). Plots of the consecutive distances between bacterial graphs (B). MDS projection of the bacterial graphs on the first two principal axes (C). Colors denote treatment phases, and shapes represent different subjects.

On an intuitive level, spanning trees are a reflection of the graph’s interconnectedness and robustness to change: to draw an analogy with electric current, this amounts to quantifying the effect of one edge deletion on the impedance of the system: how easily does the current still manage to flow?

**Application.** Interestingly, the results obtained using the spanning tree similarity are comparable to the results provided by the low-pass filter spectral distance described in the previous subsection. The spanning tree similarity also highlights comparable dynamics across subjects (Figure 7B) and the MDS projections (Figure 7C) follow a curve that enable us to do a relative comparison of states: Interim, pre-treatment and post treatment graphs are located on the extreme ends of this curve, showing the strong effect of the antibiotics on the microbiome by emphasizing the difference of these phases with respect to the treatment phases.

**Discussion.** Suppose that graph  $G$  undergoes a “small” perturbation, yielding a new graph  $\tilde{G} = \mathcal{T}(G)$ .

We know that the eigenvalues of  $\tilde{G}$  can be written as a perturbed version of the eigenvalues of  $G$ , that is:

$$\forall i, \quad \tilde{\lambda}_i = \lambda_i + \epsilon_i$$

Hence, we can write:

$$(3.3) \quad \tilde{\mathcal{T}}_G = N_{\text{Spanning tree of } \tilde{G}} = \frac{1}{N} \prod_{i=1}^{N-1} \tilde{\lambda}_i = \mathcal{T}_G \times \left[ 1 + \sum_{i=1}^{N-1} \frac{\epsilon_i}{\lambda_i} + \sum_{i,j=1}^{N-1} \frac{\epsilon_i \epsilon_j}{\lambda_i \lambda_j} + \dots \right]$$

Combining 3.3 and 3.2 yields:

$$(3.4) \quad d_{ST}(G, \tilde{G}) = \left| \log \left( 1 + \sum_{i=1}^{N-1} \frac{\epsilon_i}{\lambda_i} + \sum_{i,j=1}^{N-1} \frac{\epsilon_i \epsilon_j}{\lambda_i \lambda_j} + \dots \right) \right|$$

The impact of the change is thus inversely proportional to the value of the eigenvalues. This is an attractive property for weakly connected graphs (i.e. that have small  $\lambda_1$ ), where the addition or deletion of a critical edge can have a huge impact on the graph's overall connectivity. Conversely, changes in larger eigenvalues have less impact: to continue with the temporal frequency analogy drawn in the previous section, this similarity automatically discounts changes that are related to noise, and accentuates the impact of changes on low eigenvalues which are considered to be more reflective of the graph's structure. We emphasize that, once again, this defines a pseudo-distance between eigenspectra (or dissimilarity score between graphs), rather than a distance on the graphs themselves. This effect is shown in Figure 7, which exhibits results close to the low-pass filter approach developed in the previous subsection. The advantage of the ST dissimilarity is that it does not require the specification of a particular ad-hoc low-pass kernel on the eigenspectrum. However, this comes at an increased price in terms of the variability of the results: because the effect of perturbations is measured with respect to the inverse of the eigenvalues (Eq. 3.4), this distance is more unstable than the low-pass filter spectral distance. We will study this in more depth in our synthetic experiments in Appendix A.

We also experimentally observe that the number of spanning trees in a graph is an unstable quantity, varying by orders of magnitudes for both dense and sparse graphs generated under the same conditions: the effect of an edge's addition can considerably change the number of associated spanning trees, making the first suggested similarity in Eq. 3.4 difficult to work with. In order to account for this instability, another, more stable alternative to Kelmans's characterization of transformations by their destructive power consists in considering the following quantity:

$$(3.5) \quad d_{ST}(G, \tilde{G}) = \frac{|\mathcal{T}_G - \mathcal{T}_{\tilde{G}}|}{\frac{|\mathcal{T}_G + \mathcal{T}_{\tilde{G}}|}{2}}$$

This latter distance assesses the percentage of spanning trees that are lost (or gained) from one graph to the other, with respect to the average number of spanning trees in the two graphs. Since the previous quantity is bounded between 0 and 1, this provides a more stable pseudo-distance. We will analyze its performance on synthetic examples in Appendix A.

### 3.3. Distances based on the eigenspectrum distributions.

3.3.1. *General framework.* Rather than focusing on the graph’s eigenspectra, another alternative proposed by [20, 12] considers *continuous spectral distributions*. The continuous spectral distribution is obtained from each graph by computing the graph’s eigenvalues and considering a kernelized version of its eigenvalue distribution. For a Gaussian kernel, the spectral distribution is defined as:

$$\rho_G(x) = \frac{1}{n} \sum_{i=0}^{n-1} \frac{1}{\sqrt{2\pi\sigma^2}} e^{-\frac{(x-\lambda_i)^2}{2\sigma^2}}$$

A pseudo-distance between graphs is based on the distance between spectrum distributions, which, in the case of the  $\ell_1$ -distance used in [12], yields the following expression:

$$d(G, \tilde{G}) = \int |\rho_G(x) - \rho_{\tilde{G}}(x)| dx.$$

In their 2016 article [12], Gu and al. show that, in the limit of an infinite number of nodes, these distances have the added benefit of distinguishing between different types of graphs (Erdős-Rényi vs Preferential Attachment, etc). As such, these distances are able to recognize important geometrical information in the overall graph structure, which can make them potentially appealing for our problem at end. We now investigate a variant of such a class of distances proposed in [16] and that has been shown to exhibit interesting properties [19]: the Ipsen-Mikhailov distance.

### 3.3.2. Definition of the IM distance.

**Definition.** First introduced by Ipsen and al. [16] for graph reconstruction and later extended to the broader “graph-comparison” problem by Jurman and al [18, 19, 20], the Ipsen-Mikhailov distance is a spectral measure which relates a network on  $N$  nodes to a system with  $N$  molecules connected by elastic strings. The connections are dictated by the graph’s adjacency matrix  $A$  and the system can thus be described by a set of  $N$  equilibrium equations:

$$\frac{\partial^2 x_i}{\partial t^2} + \sum_{j \neq i} A_{ij}(x_i - x_j) = 0$$

In this setting, the eigenvalues of the Laplacian matrix of the network are interpreted as the squares of the vibrational frequencies  $\omega_i$  of the system:

$\lambda_i = \omega_i^2$  with  $\lambda_0 = \omega_0 = 0$ .

The Ipsen-Mikhailov distance characterizes the difference between two graphs by comparing *their spectral densities*, rather than the raw eigenvalues themselves. The spectral density of a graph is defined as the sum of Lorenz distributions:

$$\rho(\omega, \gamma) = K \sum_{i=1}^{N-1} \frac{\gamma}{\gamma^2 + (\omega - \omega_i)^2}$$

where  $\gamma$  is a parameter common to all vibrational frequencies that we will have to determine, and  $K$  is the normalization constant defined such that:  $\int_0^\infty \rho(\omega, \gamma) d\omega = 1$ . This spectral distance between two graphs  $A$  and  $B$  is defined as:

$$(3.6) \quad \epsilon_\gamma(A, B) = \sqrt{\int_0^\infty [\rho_A(\omega, \gamma) - \rho_B(\omega, \gamma)]^2 d\omega}$$

The latter expression depends on the choice of the scale parameter  $\gamma$ . Jurman and al. [20] set  $\gamma = \bar{\gamma}$  as the unique solution of:

$$\epsilon_{\bar{\gamma}}(\mathcal{E}_N, \mathcal{F}_N) = 1$$

So the IM distance is bounded between 0 and 1 and its upper bound is attained only for  $\{A, B\} = \{\mathcal{E}_N, \mathcal{F}_N\}$  where  $\mathcal{E}_N$  denotes the empty graph and  $\mathcal{F}_N$  the complete graph on  $N$  nodes.

**Application.** Figure 8 shows the results of the analysis of the microbiome study using the Ipsen-Mikhailov distance to our microbiome study. We note in particular that, in contrast to structural distances, the dynamics across subjects are radically different (Figure 8B). The MDS projection (Figure 8C) does not seem to pick up on either a grouping per state or per subject, which is confirmed by the lack of structure exhibited by the heat map of distances between graphs (Figure 8A). Overall, in this particular case, the Ipsen-Mikhailov distance does not seem very suited to our task: it integrates the higher eigenvalues of the spectrum, which blurs the information recovered by the low-pass filter distance exhibited in section 3.1. Such spectral distances are better suited to the comparison of graphs' overall structure without any prior on where "interesting" changes occur in the spectrum— which is not where the signal lies in this particular case. However, we note that this distance provides nonetheless better information than the vanilla identity spectral distance introduced in section 3.1: the curves in Figure 8B are more similar in shape to each other than the ones in Figure 6(B) (highlighting

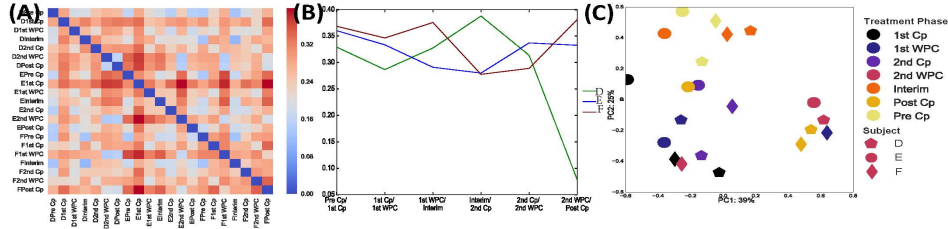


Fig 8: Application of the Ipsen-Mikhailov distance. Heatmap of the corresponding dissimilarity between Gini-correlation-based bacterial graphs (A). Plots of the consecutive distances between bacterial graphs (B). MDS projection of the bacterial graphs on the first two principal axes (C). Colors denote treatment phases, and shapes represent different subjects.

similar dynamics across subjects), and the heat map of the IM pairwise distances, Figure 8A also carries finer-grain information than for the vanilla spectral distance – in which every graph, except from E 1st Cp- seemed at uniform distance to all the others.

### 3.3.3. The Hamming-Ipsen-Mikhailov distance .

**Definition.** So far, none of these spectral distances have used the fact that particular nodes can be matched. There is no way of discriminating changes (that is, emphasizing changes in areas of the graph deemed important to the analyst), or of accounting for rare - but existing- isospectral graphs. To bridge the two approaches, Jurman and al [19] propose a distance that is a weighted linear combination of the Ipsen-Mikhailov and the normalized Hamming.

$$d_{HIM}^{\xi} = \frac{1}{\sqrt{1+\xi}} \sqrt{IM^2 + \xi H^2}$$

**Application.** The results of the microbiome analysis carried out with this distance are displayed in Figure 8. We note that the improvement with respect to the Ipsen-Mikahilov distance is only marginal.

**Discussion.** This distance benefits from the advantages of both the Hamming and the Ipsen-Mikhailov distances by combining local and global information. We emphasize that, since it is a linear combination of a distance with a non-negative quantity, this defines a proper distance between graphs. The parameter  $\xi$  provides additional flexibility to the metric by allowing to favor one type of information over another. However, empirically, we have observed this distance to be especially long to compute, and thus difficult to apply to

the study of large graphs.

### 3.4. *The Polynomial Approach.*

**Definition and motivation.** The previous spectral distances all shared a common problem: they require an explicit computation of the graph’s eigenvalues – which computational tricks aside, still generally has complexity  $O(N^3)$  – and is sensitive to global properties of the graph (as captured by the eigenvalues). Structural distances (Hamming and Jaccard) however, were too myopic in that they concentrated on changes in each node’s direct neighborhood. An other interesting line of distances would thus intermediate scale, comparing evolutions of local neighborhoods. For instance, changes in sparse regions of the graphs might be informative than perturbations in very dense ones. Following Koutra and al.’s [24] proposed guidelines for distance selection, a “good” similarity score should be able to capture such nuances and attribute more weight to changes in areas of the graphs deemed more critical by the data analyst.

In this new setup, a possible solution is to work directly with the powers of the graphs’ adjacency matrix  $A^k$ . Indeed, the powers of the adjacency matrix relate directly to a graph’s local topology through the coefficients  $A_{ij}^k$ , which corresponds to the number of paths (possibly with cycles) that start at  $i$  and arrive at  $j$  in  $k$  hops. Hence, by design, these powers are inherently local. The coefficients  $A_{ij}^k$  can be thought of as a characterization of the connectivity between two nodes with respect to the  $k$ -hop neighborhoods: nodes  $i$  and  $j$  at distance greater than  $k$  hops have connectivity index  $A_{ij}^k = 0$ , whereas nodes within each other’s  $k$ -hop neighborhood will typically have high connectivity index  $A_{ij}^k$  if the neighborhood is dense, and lower  $A_{ij}^k$  if the region is sparse. As such, the powers of the adjacency matrix seem to offer an attractive starting point to quantify changes on the mesoscale.

Typically, for each neighborhood (centered around a node  $a$ ), perturbations should be assigned weights that are monotonically decreasing functions of the distance: a perturbation has higher impact in the local neighborhood if it is closer to the center than the periphery. In this spirit, denoting as  $A_i = Q\Lambda_A Q^T$  the eigenvalue decomposition of the graph, a proposed similarity score is defined with a polynomial  $P(x) = x + \frac{1}{(N-1)^\alpha}x^2 + \dots + \frac{1}{(N-1)^{\alpha(K-1)}}x^K$  of the adjacency:

$$P(A) = QWQ^T$$

where  $W = \Lambda_A + \frac{1}{(N-1)^\alpha}\Lambda_A^2 + \dots + \frac{1}{(N-1)^{\alpha(K-1)}}\Lambda_A^K$ .



The distance between two graphs can simply be computed by taking:

$$(3.7) \quad d_{\text{pol}}(G_1, G_2) = \frac{1}{N^2} \|P(A_1) - P(A_2)\|_{2,2}$$

In a way, this distance is a straightforward extension of the Hamming distance to the mesoscale: rather than looking at perturbations at the atomic level – counting the number of removed and inserted edges without assessing the effect of the perturbation on the overall structure, this polynomial distance compares neighborhoods of larger sizes and thus attempt to capture the effect of perturbation at an intermediate scale. The weighting factor  $\alpha$  is a way of discounting “peripheral” changes in neighborhoods of larger sizes with respect to neighborhoods of smaller size. We note that Eq. 3.7 is just a proposed class of polynomial distances, but this set of distance can be more broadly customized to a specific problem at hand, including domain knowledge to choose the size of the neighborhood, etc.

**Application.** Figure 9 shows the results of the application of the polynomial distance to the microbiome data (with two different instances of polynomials). Similar to the Hamming distance, the polynomial distance does detect similar dynamics across subjects (closely matching curves in Figures 9B and 9E). We also observe a treatment-phase-wise clustering in the MDS projections (points with identical color are generally grouped in Fig.9C and 9F ). However, similarly to the vanilla eigenspectrum-based distance in section 3.1, point  $E : 1^{st}CP$  is classified as being extremely different from all the other graphs. This similarity in diagnostic with a purely spectral-based distance seems to indicate that the polynomial distance succeeds in capturing information in the overall structure of the graph. Here, it seems that the polynomial with higher discount parameter  $\alpha$  detects more structure: the curves match more closely in Figure 9B than in Figure 9E, and the heat map in Fig.9A is less uniformly blue than in Figure 9D—indicating that this distance has better discriminating power between graphs and thus captures more information. Polynomial distances thus seem to offer an attractive alternative to purely spectral distances which seem better suited to the analysis of this dataset.

**Comparison of Polynomial, Spectral and Structural distances.** The main advantage of the polynomial distances over the Hamming and Jaccard distances is that the former takes into account the properties of each node with respect to the rest of the graph. In the appendix, we show that the effect of a perturbation (that is, the addition of one edge) on the graph can be directly related to properties of the graph at a higher order than simply the one-hop neighborhood: by construction, polynomials of order  $k$  reflect the effect of the perturbation on  $k$ -hop neighborhoods. They can be expressed

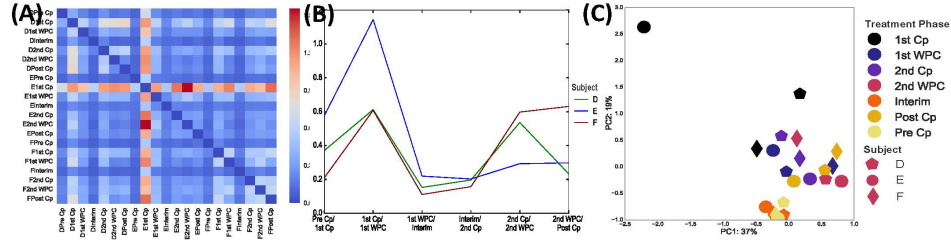


Fig 9: Application of the Polynomial dissimilarity to the microbiome bacterial graphs, for  $K = 3, \alpha = 0.9$ . Heatmap of the corresponding dissimilarity (A). Plots of the consecutive distances between bacterial graphs (B). MDS projection of the bacterial graphs (C) on the first two principal axes. Colors denote treatment phases, and shapes represent different subjects.

in terms of polynomials of the degree of the nodes of the added edge, as well as the size of the intersection of their neighborhoods (up to size  $k$ ). This is effectively a low-pass filter distance and provides a more systematic way of comparing networks by constraining the class of candidate spectral comparison functions.

#### 4. Quantifying change at the mesoscale.

The distances (aside from the polynomial distances) described in the previous section have failed our objective in some way or other: structural distances have proven to be too "local" and agnostic to perturbations' effects on a given complex system's organization as a whole. Spectral distances are too global and fail to use the information captured in the nodes' identities. Polynomial distances – which quantify changes with respect to the  $k$ -hop neighborhoods – on the other hand have shown promising properties throughout the synthetic experiments. This seems to indicate that that considerable insight is to be gained by comparing graphs at this intermediate "neighborhood" scale. This approach thus calls for the need of characterizing topological properties of these neighborhoods. In this section, we propose to investigate graph comparison through a "glocal" lense ( to borrow the expression from [19]), extending the class of mesoscale polynomial distances introduced in section 3.4 by suggesting two alternative characterizations of neighborhoods' topological properties.

##### 4.1. Quantifying interactions: connectivity-based distances.

We begin with a simple intuitive distance based on some measure of

nodes' pairwise interactions. Indeed, as previously underlined, we want a distance that: (a) preserves information about each node's identity and (b) incorporates information characterizing nodes by their relationship to the whole graphs, rather than uniquely with respect to their direct neighbors. A general framework is to consider the set of graph dissimilarities defined as:

$$(4.1) \quad d_{\text{centrality}}(G_t, G_{t+1}) = \left( \sum_{i=1}^n \sum_{j=1}^n (s_{ij}^{(t+1)} - s_{ij}^{(t)})^p \right)^{1/p}$$

where  $s_{ij}^t$  is some measure of the interaction or affinity between nodes  $i$  and  $j$  in graph  $G_t$ . This dissimilarity metric thus quantifies how much the different interactions have changed from one graph to the other. This approach satisfies our constraints in that it is both local and respects nodes' identities while accounting for the whole graph structure by summing over all pairwise "interaction" scores.

In the simplest, most intuitive case, we can simplify this expression by using centrality measures. Indeed, centrality measures (betweenness, harmonic, etc.) can typically be used to characterize them as either belonging to part of the core or the periphery of the graph, and thus encode global topological information on the status of node within the graph. These metrics thus come as natural candidates to characterize 'mesoscopic' changes. More formally, in this setting, denoting  $c_i^{(t)}$  as the betweenness-centrality of each node  $i$  in the graph at time  $t$ , one defines a distance between two graphs  $G_t$  and  $G_{t+1}$  as:

$$(4.2) \quad d_{\text{centrality}}(G_t, G_{t+1}) = \sqrt{\sum_{i=1}^n (c_i^{(t+1)} - c_i^{(t)})^2}$$

One of the positive aspects of this metric is that centrality measures are "integrated" quantities; measuring the number of paths that typically pass through a given node. As such, similarly to eigenvalues, these metrics are more robust to small perturbations in the graph structure than the Hamming distance. Moreover, each "drift" measure in Eq. 4.2 is interpretable: a change in centrality can be understood as a drift of the node away from (or towards) the core of the network. However, the problems associated with this approach are two-fold. First of all, one has to choose a single "good" centrality measure (harmonic, betweenness, etc.), which may require domain-knowledge, since this captures a specific aspect of the network's evolution. Moreover, the computation of betweenness centrality on unweighted graphs typically requires algorithms with complexity  $O(|\mathcal{V}||\mathcal{E}|)$ . This approach is thus unfortunately, like the IM distance, difficult to extend to larger graphs.

In order to make this approach more tractable, recent work has proposed using approximation algorithms to compute alternative relevant interaction metrics in Eq.4.1. For instance, in [29] Papadimitriou and al. suggest five such different scalable similarities. In [24], Koutraï and al propose a low-dimensional approximation to a loopy Belief Propagation algorithm to compute these scores – yielding a method (DeltaCon), able to approximate Eq.4.1 with a computational complexity linear on the number of edges in the graphs.

#### 4.2. Heat spectral wavelets.

Another alternative is to derive characterizations of each node’s topological properties by working directly on the graph’s spectrum. For instance, in their recent 2016 paper [28], Monning and al have proposed to build upon the DeltaCon similarity to create a (proper) distance between graphs: they introduce the Resistance Perturbation index, a metric based on the eigenvalues and eigenvectors of a modified version of the graph Laplacian. In this section, we propose to focus on using recent work in the graph signal processing literature to derive such characterizations. The approach that we propose to focus on in this subsection is span from the methodology developed in [8] for the purpose of structural role identification. In this paper, inspired by the emerging field of graph signal processing [31], the authors suggest using heat spectral wavelet to characterize each node’s local topology for the purpose of structural role identification. For the purpose of clarity, this approach is explained in further details in Appendix B.3, but on a higher level, to use a concrete analogy, this method operates in a way similar to sonar detection: each node probes the network by diffusing a heat wave, and the way that the network responds to each of these probes – that is, the different heat prints that we obtain for each node – is taken as a signature for each of the nodes’ topological neighborhoods.

Denoting  $L = U\Lambda U^T$  as the Laplacian’s eigenvalue decomposition, where  $0 = \lambda_0 \leq \lambda_1 \leq \dots \leq \lambda_{N-1}$ , the heat wavelet  $\Psi_{\cdot,a}^{(s)}$  centered at node  $a$  with scale  $s$  is defined as the column vector of the matrix  $Ue^{-s\Lambda}U^T$ :

$$\Psi_{\cdot,a}^{(s)} = Ue^{-s\Lambda}U^T\delta_a \implies \forall m, \quad \Psi_{m,a}^{(s)} = \delta_m^T Ue^{-s\Lambda}U^T\delta_a = \sum_{j=0}^{N-1} e^{-s\lambda_j} U_{aj}U_{mj}$$

where  $\delta_m$  is the indicator vector associated to node  $m$ , and  $e^{-s\Lambda}$  is the diagonal matrix  $\text{Diag}(e^{-s\lambda_0}, e^{-s\lambda_1}, \dots, e^{-s\lambda_{N-1}})$ . The authors of [8] define a structural signature for each node as the unordered set of coefficients:

$$(4.3) \quad \chi_a = \{\Psi_{m,a}^{(s)}\}.$$

By comparing these sets (or equivalently, these distributions), one captures information on the connectedness and centrality of each node within the network. Hence, these wavelet coefficients contain all the necessary information to characterize nodes' topological status within the graph. Moreover, in order to compute these wavelets in a tractable fashion that extends to large graphs, Hammond and al [13] suggest the use of Chebychev polynomial approximations. The cost of computing the wavelet transforms becomes simply  $O(K|\mathcal{E}|)$ —making spectral wavelets an attractive approach for characterizing structural roles. The trick now resides in transforming these distributions in Euclidean scores so as to plug these representations in the setting described by Eq.4.2. Appendix A.2 analyzes different ways of comparing these node distributions, but for the sake of simplicity, we propose adopting here the characteristic-function based embedding of the distributions proposed in [8] (details in Appendix B.3), which represents each distribution  $\chi_a$  by a Euclidean vector of dimension  $D$ .

The distance between graph thus amounts to an  $\ell_2$  distance between each node's structural embedding:

$$(4.4) \quad d(G_t, G_{t+1}) = \frac{1}{N} \sum_{a \in \mathcal{V}} \|r_a^{(t)} - r_a^{(t+1)}\|_2$$

To formalize the link with the previous subsection, we argue that these wavelet coefficients are in fact robust integrated centrality scores. Indeed, Chung [6] has showed that heat kernels can be understood as a robust Page Score of each node: by design, the heat kernel integrates over the neighborhoods (the size of which depends on the scale of the kernel) and is thus less sensible to small perturbations. Hence, these wavelet coefficients provide a tractable alternative to the centrality measures proposed in section 4.1. As such, they benefit from these measures' interpretability, while being generalizable to larger networks.

**Discussion.** We summarize the advantages of this method as follows.

- **tractability:** as we have already underlined, the cost of computing the wavelets via a polynomial approximation is linear in the number of edges, making it a suitable approach for large but sparse graphs.
- **granularity:** since this metric compares each node's status in the two graphs, this approach benefits from granular information which allows the possibility of identifying the nodes that have undergone the most drastic evolution. This is particularly useful in a number of applications where the identification of the area of the graph which changed the most is also of interest (what bacteria radically changed, which neurons adopted a completely different role in the graph, etc.).

- **inclusion of ‘mesoscopic’ information:** by design, the wavelets allow us to compare neighborhoods of the node at different scales automatically, thus allowing a less myopic representation to the overall graph structure than standard structural distances.

These observations also hold for the connectivity-based distances introduced in section 4.1.

4.3. *Application to the Microbiome study.* Figure 10 shows the results of the analysis of the microbiome study using a heat-wavelet based characteristic distance. We note that this distances picks up similar dynamics for subject *E* and *F*. As was seen with the Jaccard distance, *D* exhibits a slightly different trend. We also have a clear grouping of nodes by subject. We see that this distance is robust to noise levels, and indicates a clear proximity of the interim phases.

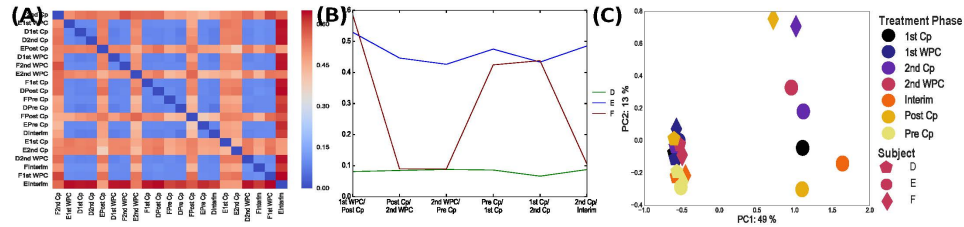


Fig 10: Application of the heat wavelet characteristic distance to the microbiome bacterial graphs, for  $s = 3$ . Heatmap of the corresponding dissimilarity (A). Plots of the consecutive distances between bacterial graphs (B). MDS projection of the bacterial graphs (C) on the first two principal axes. Colors denote treatment phases, and shapes represent different subjects.

## 5. Case study for spatial dynamics: worldwide recipe networks.

In this final section we extend the scope of our analyses from the study of temporal datasets to spatial dynamics through the study of a concrete example: a worldwide recipe network.

In this example, each different cuisine is modeled by a graph in which nodes represent ingredients, and edges measure their level of compatibility as measured by the frequency at which they co-occur in various recipes. The motivating intuition behind this graph-based representation is that cuisines can be better characterized by typical associations of ingredients rather than by an atomic analysis of the frequencies at which each ingredient appears. For

instance, the Japanese cuisine might be characterized by a higher associativity of ingredients such as “rice” and “nori” than Greek cuisine. In our analysis, the graphs were obtained by scraping 57,691 recipes from three different American culinary websites (*allrecipes*, *epicurious*, and *menupan.com*) and counting the co-occurrences of 1,530 different ingredients for 49 different cuisines (Chinese, American, French, etc.). Each cuisine is then characterized by its own co-occurrence network. A weighted edge between two ingredients corresponds to the percentage of times these ingredients simultaneously appear in a recipe out of the total number of recipes associated to that particular cuisine. The final graph for a given cuisine thus consists in a collection of disconnected nodes (ingredients that never appear in a single recipes) and a weighted connected component.

Before beginning the analysis of the different graphs, let us quickly highlight the potential challenges of this particular dataset:

- the representation of the different cuisines is highly imbalanced (Figures 11a and 11b). While the American cuisine is extremely well represented (with a little over 40,000 recipes, or 70% of the recipes), conversely, other cuisines are underrepresented: the Bangladesh cuisine, for instance, only appears 4 times in this corpus. It follows that the number of the ingredients appearing in the connected component of the co-occurrence graphs also varies substantially (Figure 11c).
- Consequently, each cuisine’s connected component only accounts for a small fraction of the 1,530 nodes (Figure 11c). As such, the distance between graphs can be considered very small and the graphs very similar, since more than 80% of the nodes are disconnected from the maximum connected component in both graphs. To account for this imbalance, the distance between cuisine  $A$  and  $B$  is computed only with respect to the ingredients appearing in either  $A$  or  $B$ ’s connected component.

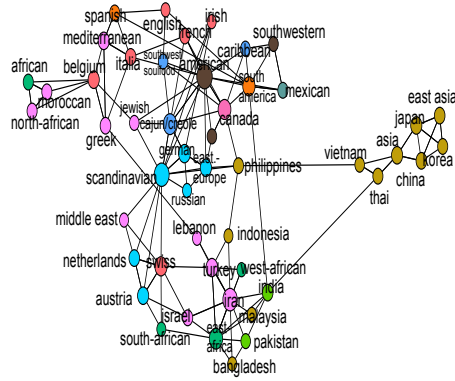
The goal of this analysis is to show the similarities captured by the different distances, and to highlight which is better suited for the comparison of the different cuisines in this very sparse and unbalanced setting. In this case, natural groupings of cuisines are relatively intuitive, and the results are thus easy to benchmark. Here, we propose to use our inferred pairwise distance matrix between ingredient co-occurrence networks and evaluate our results by both plotting the heat maps of the pairwise distances and constructing “3-nearest-cuisine summary graphs” for each type of distance. In this graph, each node corresponds to the ingredient co-occurrence network of a given cuisine  $c$ . The neighbors of cuisine  $c$  correspond to its three-nearest neighbors



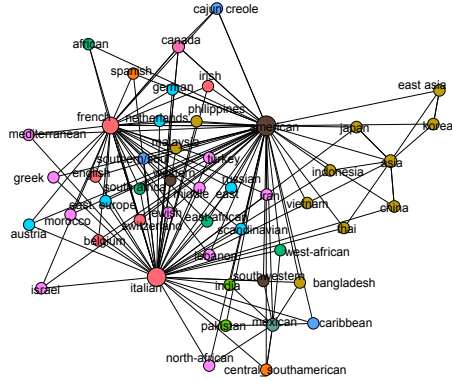


**Structural distances.**

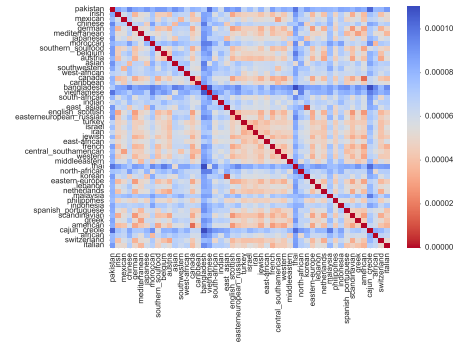
We begin by analyzing the similarities captured by the Hamming and Jaccard distances. We note that these two structural distances yield very different results. The Jaccard 3-nearest-cuisine summary graph exhibits an interesting tri-cephalic structure (Figure 12b): almost every node in the graph is connected to three main hubs (American, French and Italian). This shows that the Jaccard similarity mostly captures the proportion of shared co-occurrences (as opposed to other network properties). Indeed, here, the American, Italian and French cuisines have the largest connected components (Figure 11c), hence the overlap with the other cuisines' connected components is greater. As such, the Jaccard distance fails to recover any interesting structure in the food network. At the other extreme, the Hamming distance recovers more structure than the Jaccard distances: it manages for instance to recover clusters corresponding to East Asian and East European cuisines. We note here that the similarities are linked with the number of ingredients shared by the two cuisines. In particular, the Bangladesh cuisine – whose connected component comprises only 22 ingredients) is uniformly far from the other graphs (Figure 12c). As such, one could argue that the Hamming distance is not really more informative than the Jaccard distance, since it only reflects the overlap in connected components without accounting for the components relative sizes.



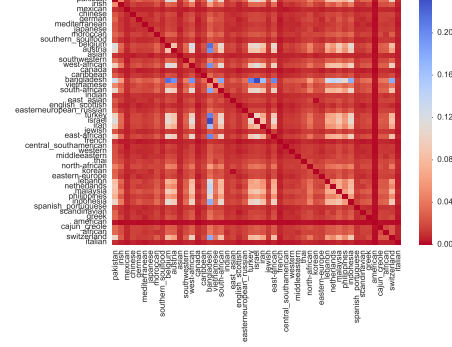
(a) 3-nearest-neighbor Proximity Graph between cuisines (Hamming Distance)



(b) 3-nearest-neighbor Proximity Graph between cuisines (Jaccard distance)



(c) Pairwise distances between cuisines (Hamming Distance)

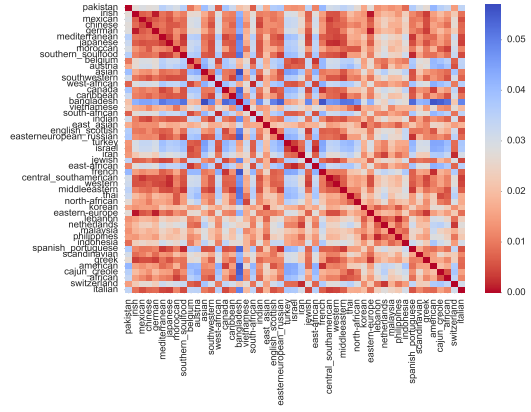
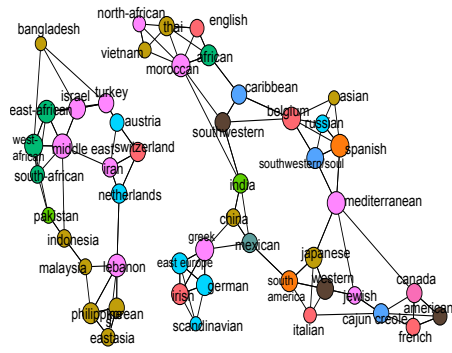


(d) Pairwise distances between cuisines (Jaccard Distance)

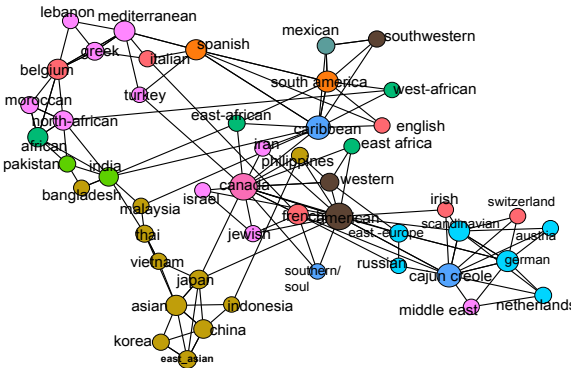
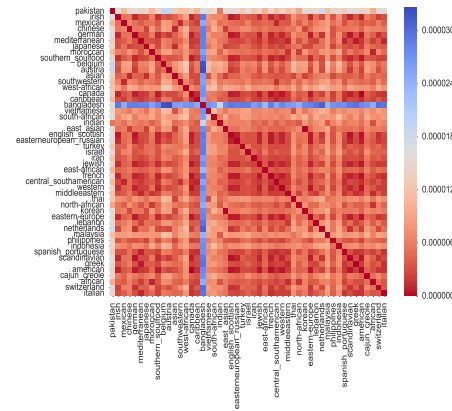
Fig 12: Comparison of the pairwise distances and three-nearest cuisine summary graphs (**Left column:** Hamming distance. **Right column:** Jaccard). The three-nearest cuisine summary graph is constructed by representing each co-occurrence network by a node and linking it to its three nearest neighbors according to a given pairwise similarity matrix.

**Spectral distances.** Spectral distances also struggle to recover similarities between cuisines. In this example, the IM and HIM yielded the same 3-nearest-neighbor graphs 13a. We note that this graph consists of two connected components, and does not follow the expected clustering of cuisines: the Mediterranean cuisines for instance (pink nodes in Figure 13a.) are scattered in each of the two clusters. This might be due to the fact that the IM distance struggles with disconnected graphs, where the eigenvalue 0 has a very high order of multiplicity for every graph: in particular, the Bangladesh graph,

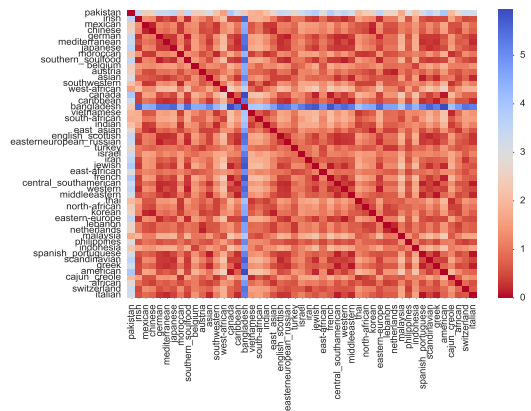
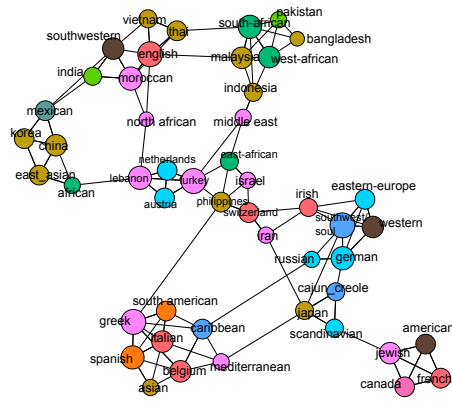
where 0 has multiplicity 1,508, is very distant from the others. In particular, we note that Bangladesh sits unusually far from America, where 0 has order of multiplicity 1,189. For the polynomial distances (Section 3.4), we have taken parameters  $\alpha = 0.9$  and  $K = 5$  ( a study of  $\alpha = 0.5$  and  $K = 3$  has achieved the same results). We have also computed a eigenspectrum-based distance (Section 3.1) with  $f(x) = e^{-0.9x}$ . In particular, the Polynomial distance seems to recover clusters that are almost consistent with geographical proximities of the different cuisines. However, the lack of structure (no block elements or pronounced groupings) apparent from the heat maps (Figures 13c and 13f) highlights the fact that spectral distances struggle to find definite patterns in this dataset. We thus conclude that a distance based on eigenvalues seems to achieve very unconvincing results for the study of graphs with many disconnected components: in this case, comparing the structure of the graph is insufficient, and we need to include information contained in the nodes' labels.



(a) 3-nearest-neighbor Proximity Graph between cuisines (Ipsen-Mikhailov Distance) (b) Pairwise distances between cuisines (Ipsen-Mikhailov Distance)



(c) Pairwise distances between cuisines (polynomial distance) (d) 3-nearest-neighbor Proximity Graph between cuisines (polynomial distance)



(e) Pairwise distances between cuisines (Eigen Distance) (f) Pairwise distances between cuisines (Eigen Distance)

Fig 13: Pairwise distances between cuisines for various spectral distances. **Top row:** Ipsen-Mikhailov distance. **2<sup>nd</sup> row:** Polynomial distance (section 3.4), with  $\alpha = 0.9$  and  $K = 5$ . **Bottom row:** Eigenspectrum-based distance (section 3.1) with  $f(x) = e^{-0.9x}$ .

**Wavelet distances.** In this case, we have computed the wavelet signatures for each node for scale  $s$  from 1 to 30 (by steps of 1). The distance was computed by comparing the characteristic signatures (obtained by sampling along the 2D parametric curve described in Eq. 6.2). Consistently with section 4, the distance between graphs  $A$  and  $B$  is simply defined as the average  $\ell_2$  distance between corresponding node’s topological signatures:

$$d_{\text{heat}}(G, \tilde{G}) = \sqrt{\frac{1}{|\mathcal{V}_G \cup \mathcal{V}_{\tilde{G}}|} \sum_{n \in \mathcal{V}_G \cup \mathcal{V}_{\tilde{G}}} (r^G(n) - r^{\tilde{G}}(n))^2}$$

where  $r^G(n)$  is the heat-kernel signature for node  $n$  in graph  $G$  as defined in section 4. The averaging ensures that we are able to compare cuisine where the number of ingredients was very different. Figure 14a shows the 3-nearest cuisine summary graph that this distance yields. We see that the graph that we are able to recover is consistent with geographical proximities would expect. We note for instance the clusters of Scandinavian cuisines and south-western European cuisines, as well as a high proximity of mediterranean cuisines and asian cuisines. It is interesting to note that this approach seems to put Bangladesh cuisine with high centrality. This is due to the limited number of recipes that we have for Bangladesh cuisine yielding more homogeneous and higher edges weights, and thus seemingly closer distance to the other graphs.

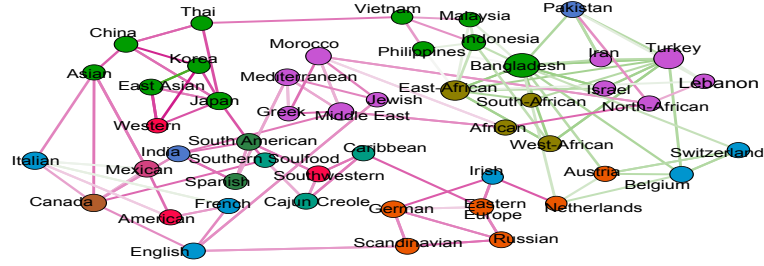
We argue that this modular approach holds considerable advantages over the prior methods since it enables us to capture in which parts of the graphs the most important changes occurs. Table 1 shows the list of 10 ingredients present in the connected components of two cuisines whose representations have changed the most (from one cuisine to the other). The first column lists the changes based on the AUC distance for a uniscale representation of the nodes (with  $s=5$ ) while the second column lists the most dramatic changes in a multi-scale representation of the nodes ( $s \in \{1, \dots, 29\}$ ) using the characteristic distance.

We also illustrate the role of the characteristic function on Figure 14b which shows how this metric can visually capture information about the relative status of each node among the different graphs. Figure 14b shows the profile of the characteristic function associated to the ingredient “almond” according to cuisines. This provides a way of visualizing differences of its uses across countries: the loopy curve of the Chinese cuisine with a relatively small projection on the  $x$ -axis can be interpreted as the fact that almonds are used in Chinese cuisine. Conversely, almonds are vastly used in Iranian and Moroccan cuisines and are thus well connected in the associated graphs, as denoted by the large projection of their curve onto the  $x$ -axis. One can imagine

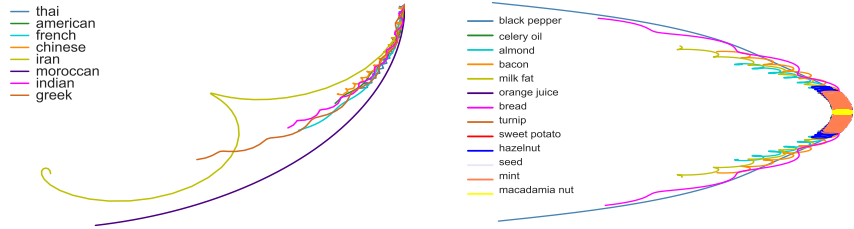
Ingredient comparisons (AUC and characteristic distances)			
Cuisine	Neighbor	top changes (AUC distance)	top changes (char. distance)
Middle Eastern	Indian	goat cheese, black tea, turkey, cocoa, cheddar cheese, cranberry, barley savory, melon, white bread	mustard, dill, bread, thyme, oregano, feta cheese, walnut sesame seed, coconut, olive
	Moroccan	apple, cranberry, brassica, artichoke, mushroom, turkey, peanut oil, coffee, banana, coconut	chive, nut, red wine, feta cheese, cane molasses, yogurt, rose, oregano, fennel, walnut
	Spanish	goat cheese, fruit, champagne wine grapefruit, banana, crab, savory sour cherry, melon, coconut	apricot, lentil, mint, zucchini walnut, pork sausage, feta cheese, sesame seed, lamb, yogurt
Chinese	Asian	malt, licorice, sour cherry, oatmeal, gruyere cheese, tarragon, savory, cognac, rum, liver	black bean, oyster, turmeric, cumin, lime juice, nira, coconut, basil, beef broth, lime
	Japanese	parmesan cheese, melon, lemon peel cocoa, lobster, orange peel, raisin, oatmeal, gelatin, milk fat	lemon, oyster, salmon, buckwheat enokidake, tuna, radish, barley, kelp, katsuobushi
	Thai	apricot, pear, parmesan cheese, buckwheat, yogurt, fruit, cheese, tarragon, kale, coffee	peanut butter, mint, roasted peanut, fenugreek, turmeric, lime juice, cumin, coconut, basil, lime

Table 1: Identification of the ingredients that change the most from one graph to another

doing the same analysis within a given cuisine, and comparing different ingredients' status. Figure 14c shows the parametric curves associated to various ingredients. We might similarly deduce that bread and black pepper are among the most common re-occurring ingredients, whereas mint and macadamia nuts are very rare.



(a) Proximity Graph between cuisines (char. distance)



(b) Characteristic signature for ingredi-ent “almond” across cuisines

(c) French cuisine: Characteristic signature of different ingredients

Fig 14: Results for the recipe-network analysis using the *heat-kernel-signature based distance*. **Top figure:** inferred 3-nearest cuisine summary graph. Colored edges denote proximity (*red*: very close. *green*: more distant.) **Bottom Row:** Visualization of the characteristic function of the same ingredient across different cuisines (left figure) and of different, randomly selected ingredients in the same cuisine (right figure). These latter plots show how characteristic signatures can help us visualize information about the relative status changes of ingredients from cuisine to cuisine.

### 6. Conclusion.

In conclusion, we have given an overview of different metrics and similarity measures for comparing graphs for which we have node labels. Our main focus has been to reflect on the types of changes and the scenarios that these distances are best suited for– highlighting these performances on both synthetic and real graph analyses.

We have illustrated the use of these metrics for analyzing sets of graphs and shown how distances are useful in assessing the variability of a dataset, or the existence of change-points. Pairwise dissimilarity matrices can also be used to draw heatmaps (and visualizing the existence – or lack-there-of– of structure in a dataset). Multidimensional scaling embeddings of graphs in Euclidean space allow us to detect latent clusters or gradients.

However, much remains to be done to construct a real framework for quantifying differences between graphs. We have not used subgraphs and

motif counts that could also be useful in quantifying such similarities as was suggested in [4]. Finding the right distance for the problem at hand can enable us to further our analyses by constructing the Fréchet mean graph or decomposing the sums of squares of distances between graphs, as was done for trees in [5]. In particular, incorporating more information about node similarities and edge lengths would enable higher resolution studies and change-point detection.



## References.

- [1] A. Banerjee. *The spectrum of the graph Laplacian as a tool for analyzing structure and evolution of networks*. PhD thesis, University of Leipzig, 2008.
- [2] A. Banerjee and J. Jost. Spectral plot properties: Towards a qualitative classification of networks. *NHM*, 3(2):395–411, 2008.
- [3] B. Bollobás. *Modern graph theory*, volume 184. Springer Science & Business Media, 2013.
- [4] A. Bonato, D. F. Gleich, M. Kim, D. Mitsche, P. Pralat, Y. Tian, and S. J. Young. Dimensionality of social networks using motifs and eigenvalues. *PLoS one*, 9(9):e106052, 2014.
- [5] J. Chakerian and S. Holmes. Computational tools for evaluating phylogenetic and hierarchical clustering trees. *Journal of Computational and Graphical Statistics*, 21(3):581–599, 2012.
- [6] F. Chung. The heat kernel as the PageRank of a graph. *PNAS*, 104(50):19735–19740, 2007.
- [7] D. B. DiGiulio, B. J. Callahan, P. J. McMurdie, E. K. Costello, D. J. Lyell, A. Robaczewska, C. L. Sun, D. S. Goltsman, R. J. Wong, G. Shaw, et al. Temporal and spatial variation of the human microbiota during pregnancy. *Proceedings of the National Academy of Sciences*, 112(35):11060–11065, 2015.
- [8] C. Donnat, M. Zitnik, D. Hallac, and J. Leskovec. Spectral graph wavelets for structural role similarity in networks. *arXiv preprint arXiv:1710.10321*, 2017.
- [9] M. Downton and T. Brennan. Comparing classifications: an evaluation of several coefficients of partition agreement. *Class. Soc. Bull.*, 4(4):53–54, 1980.
- [10] M. Ferrer, I. Bardají, E. Valveny, D. Karatzas, and H. Bunke. Median graph computation by means of graph embedding into vector spaces. In *Graph Embedding for Pattern Analysis*, pages 45–71. Springer, 2013.
- [11] A. Goldenberg, A. X. Zheng, S. E. Fienberg, E. M. Airoldi, et al. A survey of statistical network models. *Foundations and Trends® in Machine Learning*, 2(2):129–233, 2010.
- [12] J. Gu, J. Jost, S. Liu, and P. F. Stadler. Spectral classes of regular, random, and empirical graphs. *Linear algebra and its applications*, 489:30–49, 2016.
- [13] D. Hammond, P. Vandergheynst, and R. Gribonval. Wavelets on graphs via spectral graph theory. *Applied and Computational Harmonic Analysis*, 30(2):129–150, 2011.
- [14] D. K. Hammond, Y. Gur, and C. R. Johnson. Graph diffusion distance: A difference measure for weighted graphs based on the graph laplacian exponential kernel. In *Global Conference on Signal and Information Processing (GlobalSIP), 2013 IEEE*, pages 419–422. IEEE, 2013.
- [15] M. A. Hullar and J. W. Lampe. The gut microbiome and obesity. In *Obesity Treatment and Prevention: New Directions*, volume 73, pages 67–79. Karger Publishers, 2012.
- [16] M. Ipsen and A. S. Mikhailov. Evolutionary reconstruction of networks. *Physical Review E - Statistical, Nonlinear, and Soft Matter Physics*, 66(4):6–9, 2002.
- [17] J. Jost and M. P. Joy. Evolving networks with distance preferences. *Physical Review E*, 66(3):036126, 2002.
- [18] G. Jurman, M. Filosi, S. Riccadonna, R. Visintainer, and C. Furlanello. Differential network analysis and graph classification: a glocal approach. pages 1–13, 2016.
- [19] G. Jurman, R. Visintainer, M. Filosi, S. Riccadonna, and C. Furlanello. The HIM glocal metric and kernel for network comparison and classification. *Proceedings of the 2015 IEEE International Conference on Data Science and Advanced Analytics, DSAA 2015*, 7(1):46109, 2015.

- [20] G. Jurman, R. Visintainer, and C. Furlanello. An introduction to spectral distances in networks. *Frontiers in Artificial Intelligence and Applications*, 226:227–234, 2011.
- [21] G. Jurman, R. Visintainer, S. Riccadonna, M. Filosi, and C. Furlanello. A glocal distance for network comparison. *arXiv preprint arXiv:1201.2931*, 2012.
- [22] A. K. Kelmans. Comparison of graphs by their number of spanning trees. *Discrete Mathematics*, 16(3):241–261, 1976.
- [23] A. K. Kelmans. Transformations of a Graph Increasing its Laplacian Polynomial and Number of Spanning Trees. 18:35–48, 1997.
- [24] D. Koutra, N. Shah, J. T. Vogelstein, B. Gallagher, and C. Faloutsos. Deltacon: principled massive-graph similarity function with attribution. *ACM Transactions on Knowledge Discovery from Data (TKDD)*, 10(3):28, 2016.
- [25] M. Levandowsky and D. Winter. Distance between sets. *Nature*, 234(5323):34–35, 1971.
- [26] M. M. Luqman, J.-Y. Ramel, and J. Lladós. Multilevel analysis of attributed graphs for explicit graph embedding in vector spaces. In *Graph Embedding for Pattern Analysis*, pages 1–26. Springer, 2013.
- [27] C. Ma and X. Wang. Application of the gini correlation coefficient to infer regulatory relationships in transcriptome analysis. *Plant physiology*, 160(1):192–203, 2012.
- [28] N. D. Monnig and F. G. Meyer. The resistance perturbation distance: A metric for the analysis of dynamic networks. *arXiv preprint arXiv:1605.01091*, 2016.
- [29] P. Papadimitriou, A. Dasdan, and H. Garcia-Molina. Web graph similarity for anomaly detection. *Journal of Internet Services and Applications*, 1(1):19–30, 2010.
- [30] Y. Sang, X. Dang, and H. Sang. Symmetric gini covariance and correlation. *Canadian Journal of Statistics*, 44(3):323–342, 2016.
- [31] D. Shuman, S. Narang, P. Frossard, A. Ortega, and P. Vandergheynst. The emerging field of signal processing on graphs: Extending high-dimensional data analysis to networks and other irregular domains. *IEEE Signal Processing Magazine*, 30(3):83–98, 2013.
- [32] D. Shuman, B. Ricaud, and P. Vandergheynst. Vertex-frequency analysis on graphs. *Applied and Computational Harmonic Analysis*, 40(2):260–291, 2016.
- [33] D. A. Spielman. Spectral graph theory and its applications. In *Foundations of Computer Science, 2007. FOCS'07. 48th Annual IEEE Symposium on*, pages 29–38. IEEE, 2007.
- [34] M. Thüne. *Eigenvalues of matrices and graphs*. PhD thesis, University of Leipzig, 2012.
- [35] N. Tremblay et al. Graph wavelets for multiscale community mining. *IEEE TSP*, 62(20):5227–5239, 2014.
- [36] P. J. Turnbaugh, F. Bäckhed, L. Fulton, and J. I. Gordon. Diet-induced obesity is linked to marked but reversible alterations in the mouse distal gut microbiome. *Cell host & microbe*, 3(4):213–223, 2008.
- [37] P. J. Turnbaugh, R. E. Ley, M. A. Mahowald, V. Magrini, E. R. Mardis, and J. I. Gordon. An obesity-associated gut microbiome with increased capacity for energy harvest. *nature*, 444(7122):1027–131, 2006.
- [38] S. Ziebell. A powerful correlation method for microbial co-occurrence networks. Master’s thesis, The University of Arizona, 2015.

## Appendices.

### A. *Synthetic experiments: a comparison of the different distances* .

In this appendix, in order to gain a better understanding of their behavior and relative advantages, we have carried out several synthetic experiments on toy graphs. Synthetic experiments <sup>1</sup> have the benefit of offering a controlled environment to test the different distances' sensitivity relative to:

- **the graph topology:** we tested the different distances on 5 types of graphs:
  - The Erdős-Rényi model (with  $N = 85$  nodes, and a probability of connection  $p = 0.1$ )
  - a Power-Law graph on  $N = 85$  nodes (with  $\alpha = 0.9$ )
  - an Island graph (3 islands of 10 nodes, with an node-connection probability within each island of probability  $p = 0.3$  and 3 edges connecting each pair of islands)
  - a Stochastic Block Model graph, with 3 equally sampled communities and connection matrix:  $C = \begin{pmatrix} 0.4 & 0.1 & .001 \\ 0.1 & 0.2 & 0.01 \\ 0.001 & 0.01 & 0.5 \end{pmatrix}$
  - a Dot-Product graph on  $N = 85$  nodes, and randomly-sampled, normalized, gaussian feature vectors on  $K = 6$  dimensions.

These sets of network families present different global and local densities, and this study aims assess the impact of the topology on the analysis of network dynamics.

- **the perturbation mechanism:** in our first set of experiments, an initial graph is generated according to a given topology– preferential attachment, SBM, etc. We then simulate network dynamics as follows: at each time step, 15 % of the edges are removed and replugged elsewhere (uniformly at random). The aim of this study is to see how the distances behave in this simple setting: we expect the distances' curves to be stable for denser graphs, in which modifications rarely consequentially impact the structure of the graph. We might observe a bit more instability in the plots for sparser graph structures, where the deletion of a critical edge can have a much stronger impact on the overall connectivity of the graph.

---

<sup>1</sup>The code for all synthetic and real experiments developed in this review is public and available at: <https://github.com/donnate/TrackingNetworks>

- **changes in the intensity of the perturbation mechanism:** in our second set of experiments, we want to assess metrics' sensitivity to changes in the dynamical process. For the Erdős-Rényi graph, at  $T=9$ , the perturbation mechanism changes and the proportion of edges rewiring increases from 5 to 20%. For the other graphs, we tested a dynamical process with two change points. At time  $T=6$ , the perturbation level also increases from 5 to 20%. At  $T=13$ , the process reverts back to its original characteristics. The aim here is to see which distances clearly show the existence of a change-point in the graphs' dynamics.

In order to analyze the results, we propose to use (a) the Kendall correlation between distances – so as to highlight which distances exhibit similar trends and are thus sensitive to the same properties – and (b) plots of the curves showing the evolution of the graphs through time – this provides us with a way of visualizing which distances exhibit more variability and/or are best able to spot changes in the dynamics. The legend in each of the subsequent figures indicate the correspondence between curves and distances. In order to ensure an adequate visualization of all the distances despite the fact that they vary on different scales, we have normalized the observations (by their maximum observed value) so as to make them fit in the  $[0;1]$  range. The division (e.g,  $/2.39$ ) in the legend indicates the value of the normalization that was done.

#### A.1. *Structural vs Spectral distances.*

We begin by using this experimental setup to compare various instances of structural and spectral distances. The results of these experiments are summarized in figures B2, B3 and B4. We summarize our observations as follows:

- **Smooth dynamical process:** for the Erdős-Rényi graph (Figure B3-top row), most distances exhibit similar behaviors: the distance between two consecutive graphs remains constant and stable throughout the experiment. This is consistent with what is to be expected in this regime, in which the perturbation process follows the same rules as the graph generation mechanism. Changes are random, as were the initial edge assignments, and we thus do not expect the properties of the graph to change fastically throughout this experiment. Some instances of spectral distances –such as for instance the low pass-filter ( $f(x) = x\mathbb{1}_{x<2}$ ) eigenspectrum based distance– exhibit a little more variability (Figure B3-ER(E)). The main difference between distances in this experiment lies in their baseline values: the Jaccard distance

for instance has a baseline value that is almost twice as high as the Hamming distance— and is in this case, more reflective in the proportion of change in the graph structure, making it a better candidate than the Hamming distance which recovers distances that are far smaller for the much sparser PA model than in the denser SBM setting. The plots associated to the other graph topologies generally exhibit interesting increasing trends with time: the perturbation process blurs the initial topology and the graphs slowly converge to a random, Erdős-Rényi-like structure. Once again, structural distances exhibit less variability: in Figures B3, B4, B2, the Hamming, Jaccard and HIM distances stably increase. The eigenspectrum-based distances of section 3.1 (Figures B3E, B4E, and B2E), exhibit however somehow more erratic behaviors than their distributional counterparts (Ipsen-Mikhailov distance in Figures B3C, B4C, and B2C). Given the fact that the graph structure undergoes a significant continuous topological modification through time, similarities highlighting the importance of that change (such as the Polynomial or the Jaccard) seem better suited for the analysis.

- **Change-point detection problem:** We also note that most distances – except for the eigenspectrum-based methods, which are too erratic (Figures B3H, B4H, and B2H) – perform well: we are able to visually spot the time frame during which the proportion of changes increased. However, the Hamming, Ipsen-Mikhailov and HIM distances seem to be more sensible to change points occurring for dense graphs: while the change in dynamics is apparent from Figures B3-ER(F), B2-DP(F) and B4-SBM(F) for the ER, Dot Product and SBM setting, the sparsity of the PA graph seems to hinder the sensitivity of these metrics. The Spanning Tree distance also seems to struggle in the sparse setting (Island and PA graphs): its intrinsic variability makes it difficult to spot changes in dynamics. This is because in sparse settings, the structure of the graph is more vulnerable to perturbations of the adjacency matrix and the distance is thus more variable, even for small perturbation levels. We note however that it is able to spot “high-variability” zones well in denser settings (ER, SBM and Dot Product graphs in Figures B3, B4 and B2). Above all, we highlight the performance of the polynomial distances’, which, across graphs, register a bump corresponding to the high-intensity phase (Figures B3G, B2G and B4G ). The best set of candidate distances that seem to come out of this study are the Polynomial distances –which, irrespective of the topology, allow to spot two distinct regimes.
- **Link between these distances:** the analysis of the Kendall correla-

tion between these distances ( Figures B3A, B4A and B2A) highlights the correlation between the polynomial and radial kernel methods (dark red entries in the heat map for the ER, SBM and Dot Product topologies). It thus seems that the polynomial distance offers a more stable (i.e. less erratic) alternative to the eigenspectrum based distances. Interestingly enough, this effect completely subsides in sparser graphs (Island and PA graphs), where we observe a marked dichotomy between local approaches (structural and polynomial distances) and global distances (spectral distances) – as denoted by the block structure especially apparent in B4 IDa. This highlights the need for the data analyst to choose a distance suited to the topology at hand: in particular, with sparser graphs endowed with a more characteristic structure (Island or PA), the best results seems spanned by the neighborhood-sensitive polynomial distances.

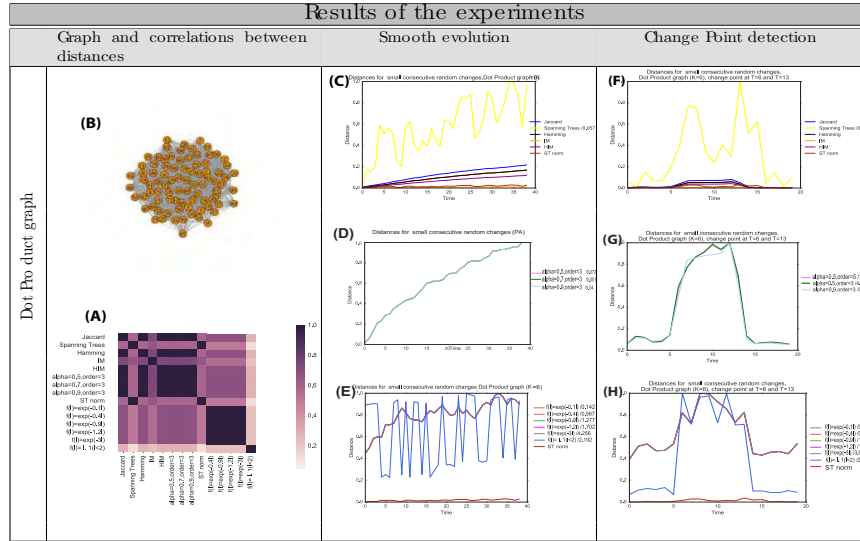
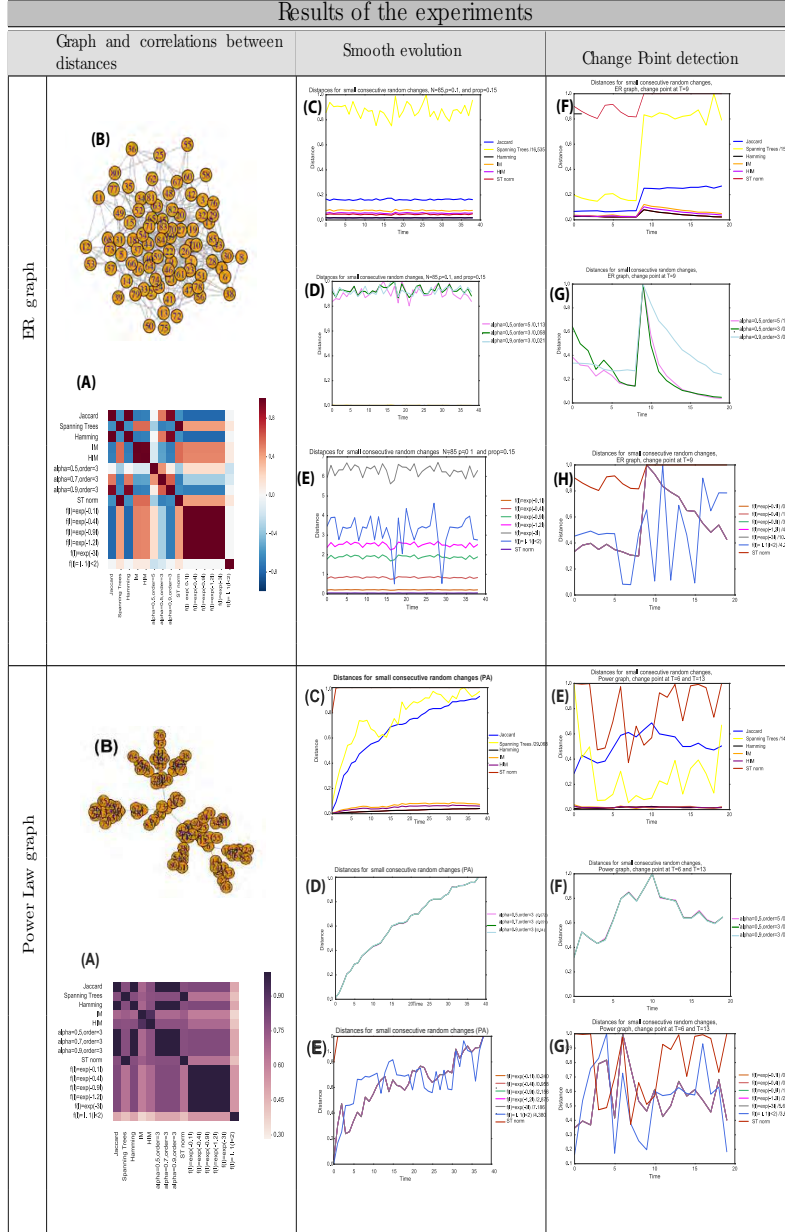


Fig B2: Results for the Dot Product Graph topology (with  $K=6$ ). **Left Column:** Comparison of the smooth dynamics (no change point), with 15% edges rewired at each time step. **Right Column:** Change point detection experiment: at time  $t = 6$ , the proportion of rewired edges increases from 15% to 20 %, and reverts to its original value at time  $t = 13$ .



1

Fig B3: Results for the Erdős-Rényi and Preferential Attachment topologies. **Left Column:** Comparison of the smooth dynamics (no change point), with 15% edges rewired at each time step. **Right Column:** Change point detection experiment (2 change points at  $t = 6$  and  $t = 13$  for the PA model, one single change point at  $t = 9$  for the ER model).

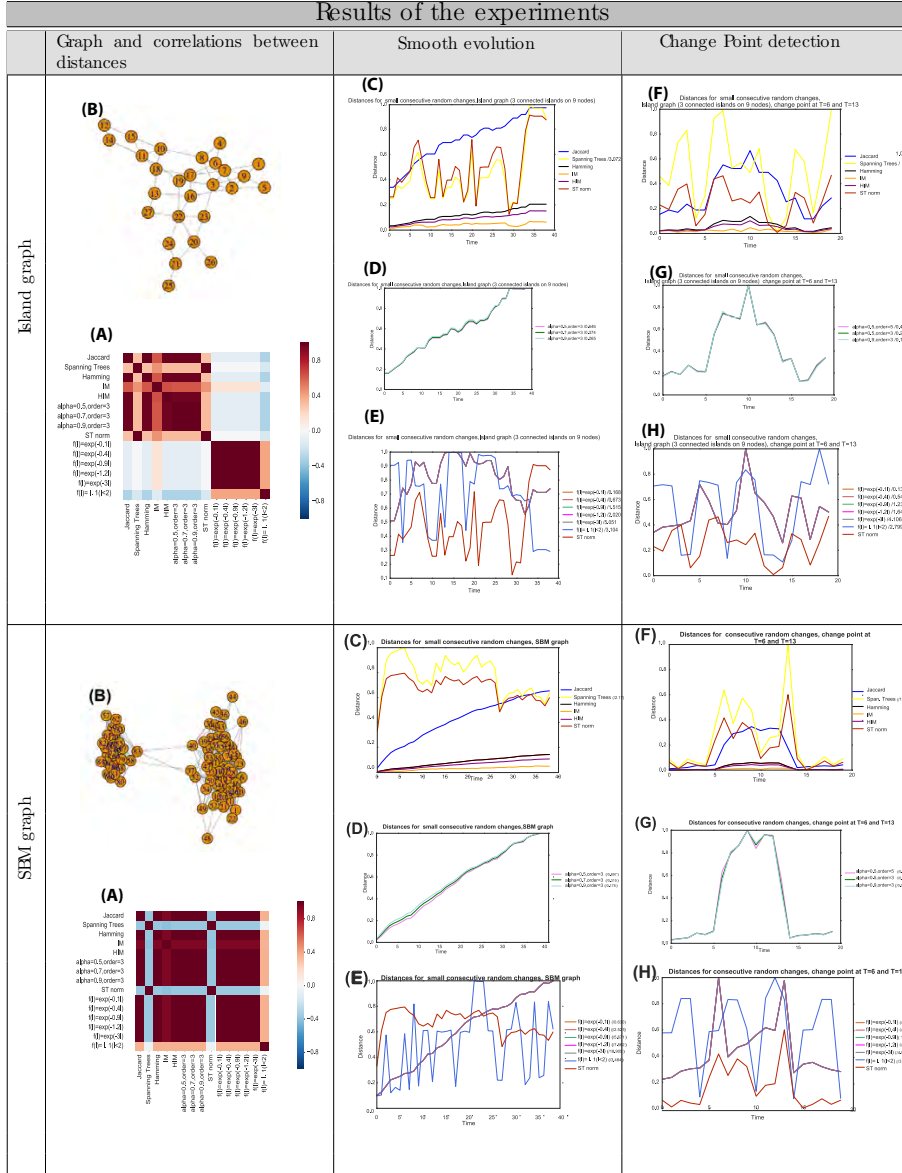


Fig B4: Results for the Island and SBM topologies. **Left Column:** Comparison of the smooth dynamics (no change point), with 15% edges rewired at each time step. **Right Column:** Change point detection experiment (2 change points at  $t = 6$  and  $t = 13$ )



### A.2. Comparing topological signatures for heat-wavelet distances.

As highlighted in section 4, the problem of comparing structural roles amounts to the problem of finding an adequate distance between the distributions that characterize each node's topological status in the graph (Eq. D8). In principle, we could choose from any off-the-shelf distance; ranging from the 2-sample Kolmogorov-distance to the Earth-Movers (Wasserstein) distance. Here, we propose to study two ways of comparing structural signatures:

- **an AUC-based distance**, corresponding to the area between the curve achieved by plotting the cumulative distribution function of each wavelet versus the other and the first diagonal. This distance thus reflects how much the curve deviates from the perfectly matching scenario. In this setting, the structural signature associated to each node is simply the vector of diffusion coefficients, ranked by increasing magnitude:

$$r_a = [\Psi_a^{(0)}, \Psi_a^{(1)}, \dots, \Psi_a^{(N-1)}]$$

where  $\Psi_a^{(0)} < \Psi_a^{(1)} < \dots < \Psi_a^{(N-1)}$ . The AUC distance is simply defined as the difference:

$$(6.1) \quad d_{AUC}(G_A, G_B) = \sum_{i=0}^{n-1} |r_A^{(i+1)} - r_A^{(i)}| \times |r_B^{(i+1)} - r_B^{(i)}| - |r_A^{(n)} - r_A^{(0)}| \times |r_B^{(n)} - r_B^{(0)}|$$

- **a characteristic-function based distance**, that is, an  $\ell_2$  distance between Euclidean embeddings of these distributions. Indeed, in [8], the authors propose an embedding of the wavelet distribution in a real-valued vector - thus allowing these objects to be easier to work with. Their approach is as follows: for a given diffusion, it can be easily shown that all the wavelet coefficients sum to one and are non-negative. The wavelets can thus be understood as a probability distribution over the nodes. Since the characteristic function of a probability distribution  $X$  - defined as the function  $\phi_X(t) = \mathbb{E}[e^{itX}]$ ,  $t \in \mathbb{R}$  completely specifies the distribution  $X$ , it provides an attractive characterization of the wavelets in terms of two-dimensional parametric curves. The empirical characteristic function of each wavelet is:

$$(6.2) \quad \forall t \in \mathbb{R}, \quad \phi_{s,a}(t) = \frac{1}{N} \sum_{m=1}^N e^{it\Psi_{m,a}^{(s)}}.$$

Hence, an alternative representation of a node's topological signature can be achieved by sampling along the 2D parametric curve induced by

(6.2) at points  $t_1 < \dots < t_n \in \mathbb{R}^+$ , and concatenating the values of the characteristic function at points  $(t_i)_{i \in [1, n]}$  into a  $2n$  dimensional vector:

$$(6.3) \quad r_a = \left( \text{Re}(\phi_{s,a}(t_i)), \text{Im}(\phi_{s,a}(t_i)) \right)_{t_1, \dots, t_n} \in \mathbb{R}^{2n}.$$

We note that this has the advantage of integrating “multiscale” information and comparing neighborhoods of different radii: we can indeed extend this signature to include information for  $J$  different values of the scale by stacking representations, thus giving us a ‘multiscale characterization of the neighborhoods:

$$(6.4) \quad r_a = \left( \text{Re}(\phi_{s_j,a}(t_i)), \text{Im}(\phi_{s_j,a}(t_i)) \right)_{s_1, \dots, s_J, t_1, \dots, t_n} \in \mathbb{R}^{2nJ}.$$

In this setting, considering a given node  $a$  in a graph  $G_t$  at time  $t$  and denoting its structural signature at time  $t$  as  $r_a^{(t)}$ , the structural change that it undergoes is given by:

$$d(a^{(t)}, a^{(t+1)}) = \|r_a^{(t)} - r_a^{(t+1)}\|_2$$

A distance between graphs can be achieved by aggregating the nodes’ individual changes:

$$(6.5) \quad d(G_t, G_{t+1}) = \frac{1}{N} \sum_{a \in \mathcal{V}} \|r_a^{(t)} - r_a^{(t+1)}\|_2$$

We begin by comparing the performance of the AUC distance to the characteristic distances on synthetic data. Our goal here is to illustrate the ability of these heat-wavelet distances to capture similarities between graphs and to detect changes in dynamics. As in the previous section, we assess the performance of the heat wavelet for different graph topologies, and for different values of the scale parameter  $s$ .

**Continuous Regime.** We begin by assessing the performance of the spectral-heat-wavelet distance in a continuous regime. The left-hand side column corresponds to the analysis led using the characteristic distance (denoted as “chi”) at various scales (Eq.6.3), including a multiscale version (Eq.6.4, denoted as “chi agg” on the figures). The right column corresponds to the analog obtained using the AUC distance defined in Eq. 6.1. Our goal here is to compare in particular the variability of the AUC and characteristic-function based distances. Indeed, in order to correctly capture change points in dynamics, we need consecutive distances within each dynamic phase to stable and be centered around a certain value: “jumps” in consecutive distance

would thus be truly indicative of dynamical changes— rather than inherent variability of the metric. In order to evaluate this variability, we compute the empirical distribution of consecutive distances.

We summarize our observations as follows:

- For the ER graph (Figure B5 top row), both the AUC and characteristic-function based distances exhibit similar, stable values: the curves showing the distances between consecutive graphs are smooth in both cases ( Figures B5 C and D), especially for large scales. We note that smaller scale values —corresponding to smaller neighborhood sizes— yield higher distances between graphs. Interestingly, the AUC exhibits less variability than the characteristic-function based distance.
- As the scale increases, the characteristic distance becomes less and less sensitive to the changes in structure (flatter and flatter curves for the consecutive distances). This is consistent with the fact that the wavelet distributions converge to the uniform distribution as the scale increases: the heat propagates over the network, and the system converges to a consensus state where all the nodes have identical temperature.
- For the other topologies, the AUC distance generally yields less variable distances with a generally greater signal-to noise ratio (Figures B5B/F, B6B/F and B7B/F) — an attractive quality with respect to the somehow more erratic characteristic distances. However, in general, AUC distances do not deviate from their original baseline: the consecutive distance plots remain flat regardless of the initial topology. On the other hand, similarly to the Polynomial distances of section 3.4, the characteristic distances exhibit an increasing trend, highlighting the fact that the graph structure strongly varies throughout the process. The characteristic-function based distance seems to be the most stable in dense graphs ( B7A).

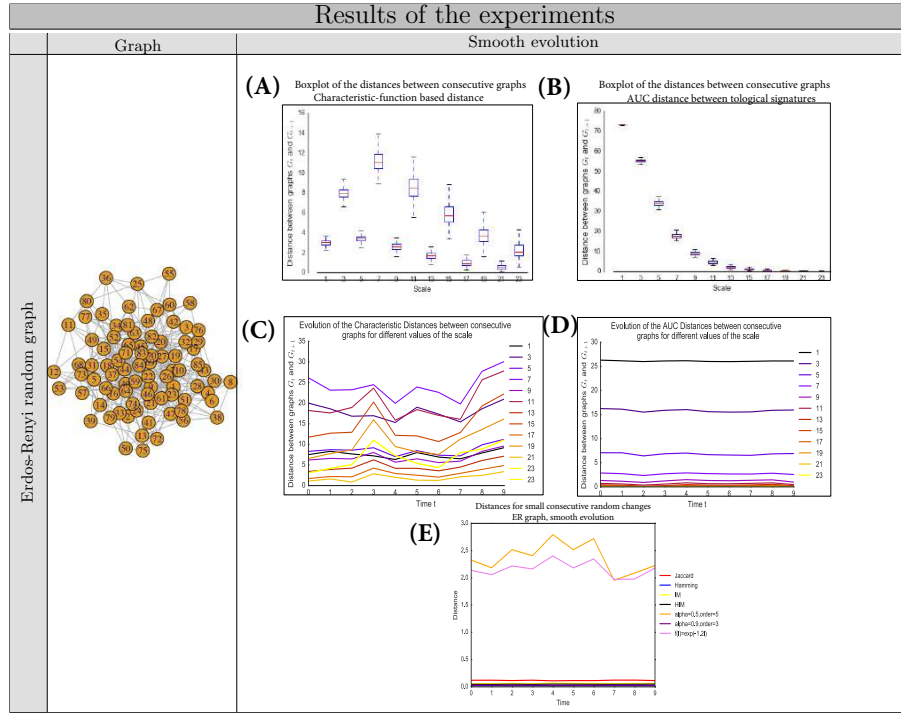


Fig B5: Results for the synthetic “smooth random changes” experiments for the Erdős-Rényi graph. Boxplots of the distribution of distances between consecutive graphs ( $N=80$  nodes,  $p=0.2$ ) averaged over 60 samples) for (A) the characteristic-function based distance and (B) the AUC distance. The “chi-agg” has been divided by the number of scales it takes into account to be comparable to the other box plots. Distances between consecutive graphs ( $N=85$  nodes,  $p=0.4$ ) for different values of the scale parameter for (C) the characteristic-function based distance, (D) the AUC distance, and (E) for standard distances (as introduced in section 2 and 3).

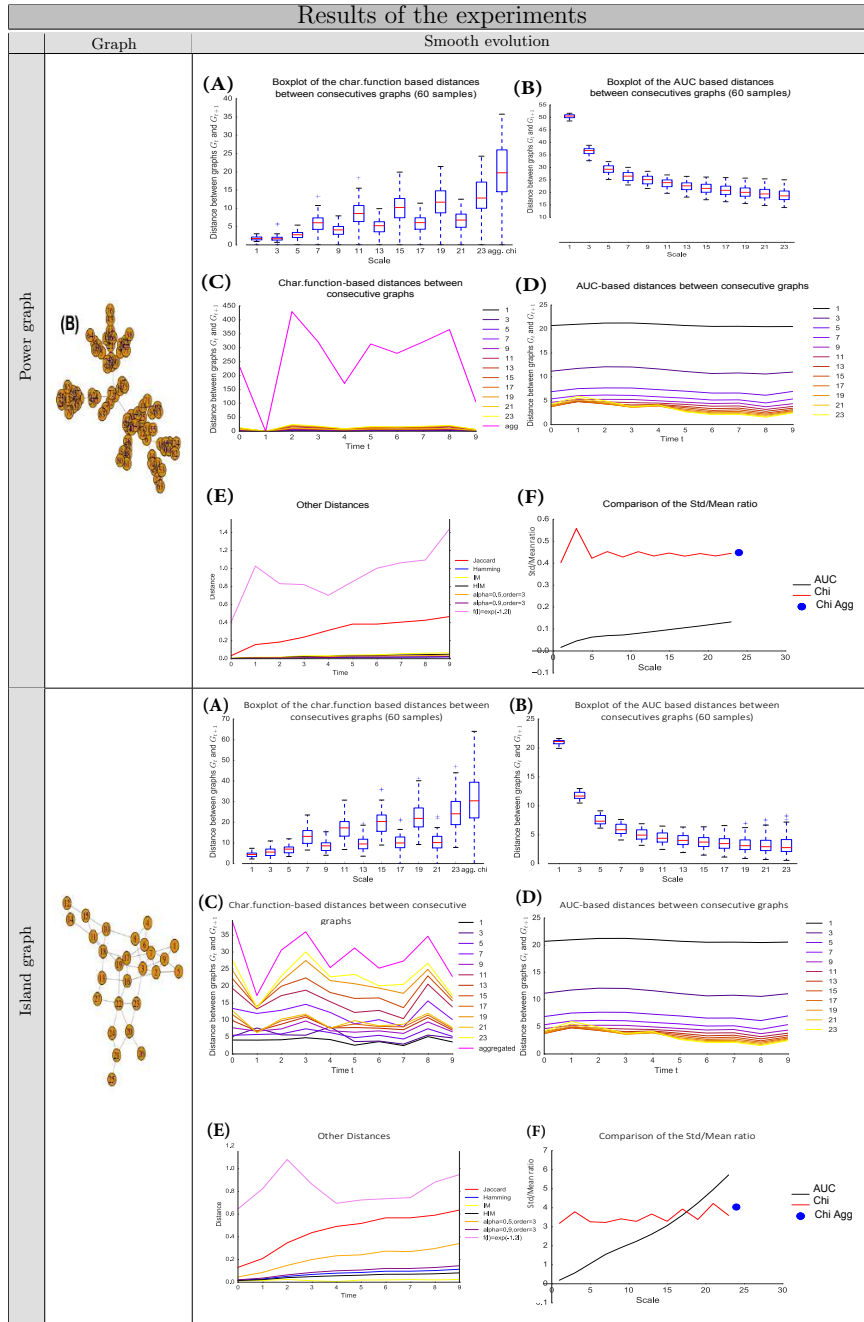


Fig B6: Results for the synthetic “smooth random changes” experiments for the Island Graph and Preferential attachment models. Boxplots of the distribution of distances between consecutive graphs (averaged over 60 samples) for (A) the characteristic-function based distance and (B) the AUC distance. Distances between consecutive graphs for different values of the scale parameter for (C) the characteristic-function based distance, (D) the AUC distance, and (E) for standard distances (as introduced in section 2 and 3). (F) Plot of the standard deviation over mean ratio as the scale increase.

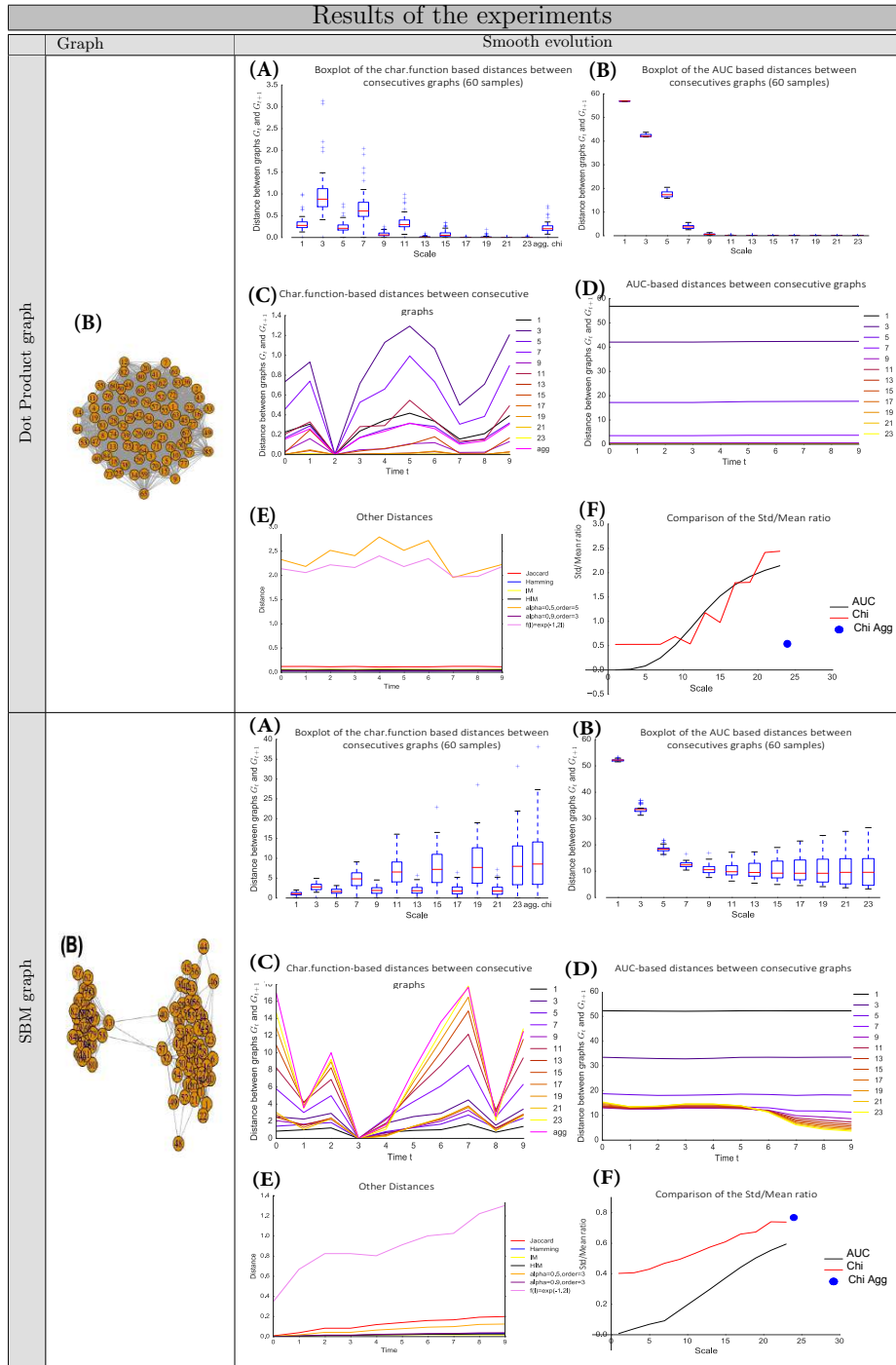


Fig B7: Results for the synthetic “smooth random changes” experiments for the Dot Product and SBM models. Boxplots of the distribution of distances between consecutive graphs (averaged over 60 samples) for (A) the characteristic-function based distance and (B) the AUC distance. Distances between consecutive graphs for different values of the scale parameter for (C) the characteristic-function based distance, (D) the AUC distance, and (E) for standard distances (as introduced in section 2 and 3). (F) Plot of the standard deviation over mean ratio as the scale increases.

### Change point detection Problem.

We now evaluate the wavelet-based distances ability to capture changes in dynamics. The results of the experiments are summarized in figures B9, B10.

Overall, the two distances (AUC and characteristic distance) allow a good visualization of the changes in dynamics (figures B9B/C, B10B/C). Interestingly, the characteristic distance seems to be a little more sensitive to the change in than the AUC: the “low-variability” zone exhibits spikes in the characteristic-function distance that are smaller with respect to the “high-variability” zone (Figures B9B, B10B) than their AUC-based counterparts.

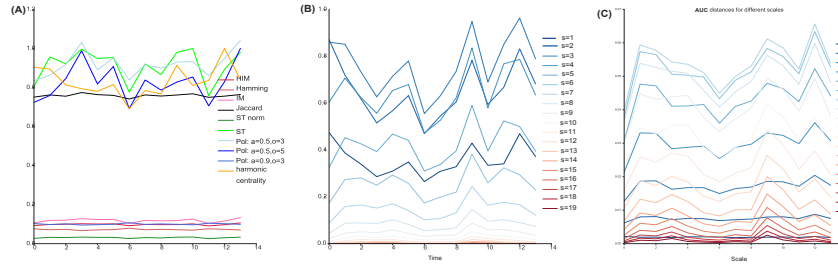


Fig B8: **(A)** Benchmark of “standard” distances (see sections 2 and 3) between consecutive graphs for different scales, for smooth random dynamics (ER graph). The spanning tree distance (ST) and harmonic centrality distances have been scaled to the  $[0,1]$  range to enable comparisons. **(B)** / **(C)** Characteristic distances/AUC distances between consecutive graphs for different scales, for smooth random dynamics (ER graph)

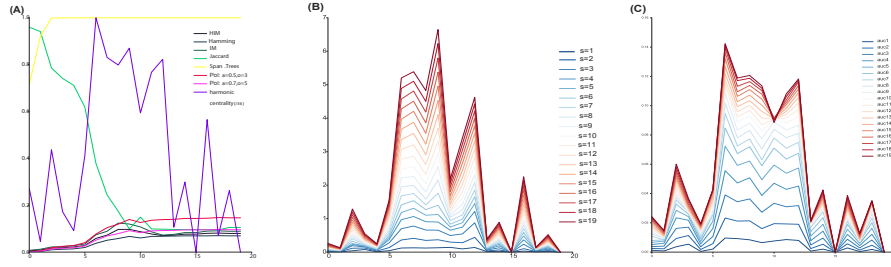


Fig B9: Change-point detection on a Preferential Attachment graph (as described in the beginning of Appendix A) using (A) standard metrics (described in section 2 and 3) and spectral wavelet characterizations with (B) the characteristic-function based distance and (C) the AUC distance.

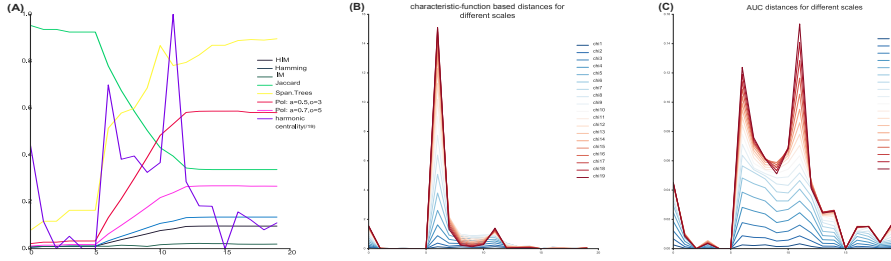


Fig B10: Change-point detection on a SBM graph (as described in the beginning of Appendix A) using (A) standard metrics (described in section 2 and 3) and spectral wavelet characterizations with (B) the characteristic-function based distance and (C) the AUC distance.

### A.3. Mesoscale distances vs “Standard distances”.

We now compare the heat-wavelet distances with the distances introduced in sections 2 and 3. It appears from Figures B9 and B10 that these spectral-wavelet distances exhibit interesting traits with respect to their standard counterparts (B8A, B9A, B10A). In particular, they seem to perform better in detecting changes in dynamic regimes. We also note that the shape of the heat-wavelet-based distance curve is similar to the harmonic-centrality based metric. Moreover, these metrics are the only ones able to “recover” from the second change point: most of the over distances remain at higher levels than in the first part of the experiment ( $t \in [0, 6]$ ). This is due to the fact that the topology of the graphs have changed during the high-variability period, and



most distances thus cannot revert to their initial baseline values. In contrast, the characteristic distance is able to recognize similar dynamics in the two parts of the time series. As such, the wavelet approach seem to provide a scalable alternative to a connectivity-score based distance (section 4.1) based on the harmonic centrality of the different nodes (Eq.4.2). Overall, looking at these plots, it seems that this approach offers attractive traits for detecting changes in dynamics (with respect to the other methods).

B. *Additional distance characteristics and comparisons.*

In this appendix, we propose to dig deeper into the characterization and properties some of the distances described in this paper – which, for the purpose of clarity, we have not included in the main body of the article.

B.1. *Ipsen-Mikhailov distance.*

We come back to the definition of the Ipsen-Mikhailov distance provided in Eq. 3.6 . The main drawback of this characterization is that it relies on two parameters,  $K$  and  $\gamma$ , whose values can be approximated but for which the literature (to the best of our knowledge) does not provide any reference – giving this interesting metric a black-box flavor. To be more explicit and understand how this distance behaves for different types of graphs, let us explicitly determine approximations (in the limit of large  $N$ ) of its parameters. **Normalization constant  $K$ .** To begin with, the normalization constant can be written as:

$$\begin{aligned}
 (D2) \quad K \int_0^\infty \rho(\omega, \gamma) d\omega = 1 &\iff K \sum_{i=1}^{N-1} \int_0^\infty \frac{1}{\gamma} \frac{1}{1 + \left(\frac{\omega - \omega_i}{\gamma}\right)^2} d\omega = 1 \\
 &\iff K \sum_{i=1}^{N-1} \underbrace{\left[ \arctan\left(\frac{\omega - \omega_i}{\gamma}\right) \right]_0^\infty}_{=\pi/2 + \arctan(\omega_i/\gamma)} = 1 \\
 &\iff K = \frac{1}{(N-1)\frac{\pi}{2} + \sum_{i=1}^{N-1} \arctan(\omega_i/\gamma)}
 \end{aligned}$$

This yields:

- **for the empty graph  $\mathcal{E}_n$** , which has eigenvalue 0 with multiplicity  $N$ :

$$K_{\mathcal{E}_n} = \frac{1}{\frac{(N-1)\pi}{2}}$$

- **for the complete graph  $\mathcal{F}_n$** , where  $\omega_0 = 0$ , and  $\omega_1^2 = \dots =$

$$\omega_{N-2}^2 = \omega_{N-1}^2 = N:$$

(D3)

$$\begin{aligned} K_{\mathcal{F}_n} &= \frac{1}{(N-1)(\frac{\pi}{2} + \arctan(\sqrt{N}/\gamma))} = \frac{1}{(N-1)(\pi - \arctan(\gamma/\sqrt{N}))} \\ &= \frac{1}{(N-1)(\pi - \gamma/\sqrt{N}[1 - \frac{1}{3}(\gamma^2/N) + o(1/N)])} \\ &= \frac{1}{(N-1)\pi} [1 + \frac{\gamma}{\pi\sqrt{N}} [1 - \frac{1}{3}\frac{\gamma^2}{N} + o(\frac{1}{N})]] + \frac{\gamma^2}{\pi^2 N} + \frac{\gamma^3}{\pi^3 N^{3/2}} + o(\frac{1}{N^{3/2}})] \\ &= \frac{1}{(N-1)\pi} [1 + \frac{\gamma}{\pi\sqrt{N}} + o(\frac{1}{\sqrt{N}})] \end{aligned}$$

Hence:

$$(D4) \quad \boxed{K_{\mathcal{F}_n} \approx \frac{1}{2} K_{\mathcal{E}_n}}$$

**The Intuition behind the Scale Parameter.** Through properties of the Lorenz distribution, the scale parameter  $\gamma$  is equal to half the interquartile range. It is thus a measure of the “probable measurement error” with respect to the mode  $\omega_i$ . Here, as proposed by [19], we have chosen  $\gamma$  such that the spectral distance between the empty graph and the complete graph is 1:  $\epsilon_{\gamma}(\mathcal{E}_N, \mathcal{F}_N) = 1$ . By definition of the Ipsen-Mikhailov distance, and using Eq.D4 to estimate the different normalizing constants:

(D5)

$$\begin{aligned} \rho_{\mathcal{F}_N}(\omega, \gamma) - \rho_{\mathcal{E}_N}(\omega, \gamma) &= \frac{N-1}{\gamma} K_{F_n} \left[ \frac{1}{(\frac{\omega-\sqrt{N}}{\gamma})^2 + 1} - \frac{2}{(\frac{\omega}{\gamma})^2 + 1} \right] \\ &= \frac{N-1}{\gamma} K_{F_n} \left[ \frac{\gamma^2}{N} \frac{1}{1 - 2\frac{\omega}{\sqrt{N}} + \frac{\omega^2}{N} + \frac{\gamma^2}{N}} - \frac{2}{(\frac{\omega}{\gamma})^2 + 1} \right] \\ &= \frac{1}{\pi\gamma} \left( \frac{\gamma^2}{N} [1 - \frac{2\omega}{\sqrt{N}} + o(\frac{1}{N^{1/2}})] - \frac{2}{(\frac{\omega}{\gamma})^2 + 1} \right) \quad \text{since } (N-1)K_{F_n} \approx \frac{1}{\pi} \\ &= \frac{1}{\pi\gamma} \left[ -\frac{2}{(\frac{\omega}{\gamma})^2 + 1} \right] + o(\frac{1}{N}) \end{aligned}$$

Hence:

$$\begin{aligned}
\int_0^\infty [\rho_{\mathcal{F}_N}(\omega, \gamma) - \rho_{\mathcal{E}_N}(\omega, \gamma)]^2 d\omega &= \int_0^\infty \frac{1}{\pi^2 \gamma^2} \frac{4}{\left(\left(\frac{\omega}{\gamma}\right)^2 + 1\right)^2} d\omega + o\left(\frac{1}{N}\right) \\
\text{(D6)} \qquad \qquad \qquad &= \frac{4}{\pi^2 \gamma} \frac{1}{2} \left[ \frac{\omega \gamma}{\omega^2 + \gamma^2} + \arctan\left(\frac{\omega}{\gamma}\right) \right]_0^\infty \\
&= \frac{1}{\pi \gamma}
\end{aligned}$$

Hence, here:  $\bar{\gamma} \approx \frac{1}{\pi}$

### B.2. Comparison with other spectral distances.

The advantages Ipsen-Mikhailov distance has two advantages over the other spectral distances: it has a “physical” interpretation as the joint behavior of a system on  $N$  strings. Secondly, empirically, it outperforms other spectral distances in capturing regime changes in the dynamics of the network (see the experiments detailed in section ??). However, the running time required by this distance increases dramatically with the number of nodes, making it a less practical tool to work with on large graphs.

The advantages of the Ipsen-Mikhailov distance over the spectral distances previously introduced is linked to its use of the  $\ell_2$  norm of the spectral densities rather than raw eigenvalues themselves: the integration of this density makes the distance more robust to small perturbations that have little structural effect, making this distance more appropriate to the analysis of complex systems.

We can assess the impact of the perturbation of a graph  $G$ , with adjacency matrix  $A$ . By supposing that the perturbation is small enough that each vibration frequency  $\omega_i = \sqrt{\lambda_i}$  of the Laplacian is perturbed by an amount  $\epsilon_i$ . Writing  $\tilde{\omega}_i = \omega_i + \epsilon_i$ , we have:

$$\begin{aligned}
\frac{1}{\left(\frac{\omega - \omega_i - \epsilon}{\gamma}\right)^2 + 1} &= \frac{1}{\left(\frac{\omega - \omega_i}{\gamma}\right)^2 + 1 - \frac{2\epsilon(\omega - \omega_i)}{\gamma^2} + \frac{\epsilon^2}{\gamma^2}} = \frac{1}{\left(\frac{\omega - \omega_i}{\gamma}\right)^2 + 1 - \frac{2\epsilon}{\gamma^2} \left((\omega - \omega_i) - \frac{\epsilon}{2}\right)} \\
&= \frac{1}{\left(\frac{\omega - \omega_i}{\gamma}\right)^2 + 1} \left[ 1 + \frac{\frac{2\epsilon}{\gamma^2} \left((\omega - \omega_i) - \frac{\epsilon}{2}\right)}{\left(\frac{\omega - \omega_i}{\gamma}\right)^2 + 1} + 4 \frac{\epsilon^2 (\omega - \omega_i)^2}{\gamma^4 \left(\left(\frac{\omega - \omega_i}{\gamma}\right)^2 + 1\right)^2} + o(\epsilon^2) \right] \\
&= \frac{1}{\left(\frac{\omega - \omega_i}{\gamma}\right)^2 + 1} \left[ 1 + \frac{2\epsilon(\omega - \omega_i)}{\gamma^2 \left(\left(\frac{\omega - \omega_i}{\gamma}\right)^2 + 1\right)} \right. \\
&\quad \left. - \frac{\epsilon^2}{\gamma^2 \left(\left(\frac{\omega - \omega_i}{\gamma}\right)^2 + 1\right)} \left[ 1 - 4 \frac{(\omega - \omega_i)^2}{\gamma^2 \left(\left(\frac{\omega - \omega_i}{\gamma}\right)^2 + 1\right)} \right] + o(\epsilon^2) \right]
\end{aligned}$$

Hence, the IM distance between the spectra of graphs  $G$  and  $\tilde{G}$  becomes:

$$\begin{aligned}
& \int_0^\infty \left[ \frac{1}{\left(\frac{\omega - \omega_i - \epsilon_i}{\gamma}\right)^2 + 1} - \frac{1}{\left(\frac{\omega - \omega_i}{\gamma}\right)^2 + 1} \right]^2 d\omega \\
&= \int_0^\infty \frac{4\epsilon^2}{\gamma^2} \frac{1}{\left[\left(\frac{\omega - \omega_i}{\gamma}\right)^2 + 1\right]^4} \left[ \frac{(\omega - \omega_i)}{\gamma} \right]^2 d\omega + o(\epsilon^2) \\
&= \int_{-\omega_i/\gamma}^\infty \frac{\gamma 4\epsilon^2}{\gamma^2} \frac{x^2}{[x^2 + 1]^4} dx + o(\epsilon^2) \\
&= \frac{4\epsilon^2}{\gamma} \times \frac{1}{2 \times 48} \left[ \frac{(x(-3 + 8x^2 + 3x^4))}{(1 + x^2)^3} + 3\arctan[x] \right]_{-\omega_i/\gamma}^\infty + o(\epsilon^2) \\
&= \frac{\epsilon^2}{24\gamma} \left[ 3\pi/2 - (3\arctan(-\omega_i/\gamma) - \frac{(\omega_i/\gamma)(-3 + 8(\omega_i/\gamma)^2 + 3(\omega_i/\gamma)^4)}{(1 + (\omega_i/\gamma)^2)^3}) \right] + o(\epsilon^2) \\
&= \frac{\epsilon^2}{16\gamma} \left[ \pi + 2\arctan(\omega_i/\gamma) + \frac{2(\omega_i/\gamma)(-3 + 8(\omega_i/\gamma)^2 + 3(\omega_i/\gamma)^4)}{3(1 + (\omega_i/\gamma)^2)^3} \right] + o(\epsilon^2) \\
&= \frac{\epsilon^2}{16\gamma} \left[ \pi + 2\arctan(\omega_i/\gamma) + \frac{2(\omega_i/\gamma)}{3} \left[ \frac{-8}{(1 + (\omega_i/\gamma)^2)^3} + \frac{2}{(1 + (\omega_i/\gamma)^2)^2} \right. \right. \\
&\quad \left. \left. + \frac{3}{1 + (\omega_i/\gamma)^2} \right] \right] + o(\epsilon^2)
\end{aligned}$$

Summing over all perturbed eigenvalues and taking the square root yields:

$$d_{IM}(A, \tilde{A}) \propto \sqrt{\sum_i \epsilon_i^2} + o(\|\epsilon\|_2)$$

and the variations are of the order  $\|\epsilon\|_2$ . By comparison, provided that the perturbation of each frequency  $\omega_i$  is small enough and since  $\tilde{\lambda}_i = \lambda_i + 2\epsilon_i\sqrt{\lambda_i} + \epsilon_i^2$ , from Eq. 3.1, the standard  $\ell_p$ -distances are such that:

$$d(A, \tilde{A})^p = \sum_{i=1}^{N-1} |2\sqrt{\lambda_i}f'(\lambda_i)|^p \epsilon_i^p + o\left(\sum_{i=1}^{N-1} \epsilon_i^p\right).$$

As such, the distance between  $G$  and  $\tilde{G}$  puts more emphasis on changes in the eigenspectrum where the product  $\sqrt{\lambda_i}f'(\lambda_i)$  is large – which might result in putting too much weight on “noisy” components of the signal, to continue with the signal frequency analogy of section 3.1. Moreover, if we now want to compare the IM distance with the spanning tree distance, we note that the

spanning tree (ST) distance is such that:

$$\begin{aligned} d_{ST}(A, \tilde{A}) &= \sum_{i=1}^{N-1} |\log(\lambda_i + \epsilon_i^2 + 2\sqrt{\lambda_i}\epsilon_i) - \log(\lambda_i)| \\ &= \sum_{i=1}^{N-1} \left| \log\left(1 + \frac{\epsilon_i^2}{\lambda_i} + \frac{2\epsilon_i}{\sqrt{\lambda_i}}\right) \right| \approx \sum_{i=1}^{N-1} \frac{\epsilon_i}{\sqrt{\lambda_i}} \quad (**) \end{aligned}$$

where (\*\*) holds provided that the perturbation remains small compared to the magnitude of the corresponding eigenvalues. However, in the case of sparse graphs, the second smallest eigenvalue (the algebraic connectivity of the graph) is typically very small (and bounded below by  $\frac{4}{ND}$  where  $D$  is the diameter of the graph). This eigenvalue might thus actually be of the order of the perturbation, thus yielding high variability in the proposed log-ST distance.

The interpretation for the good performance of the Ipsen-Mikhailov distance as embedding the distances between graphs in a probabilistic setting, where we compare distributions over eigenvalue densities, explains its increased robustness to small changes or local perturbations.

**B.3. Heat Wavelet characteristics.** We propose to introduce in this appendix in more details the spectral heat wavelet signatures that were introduced in section 4.

**Spectral heat wavelets.** We begin by introducing the concept of spectral graph wavelets, as proposed by [14, 31] and adapted for topological probing in [8]. Denoting  $L = U\Lambda U^T$  as the Laplacian's eigenvalue decomposition, where  $0 = \lambda_0 \leq \lambda_1 \leq \dots \leq \lambda_{N-1}$ , the heat wavelet  $\Psi_{\cdot,a}^{(s)}$  centered at node  $a$  with scale  $s$  is defined as the column vector of the matrix  $Ue^{-s\Lambda}U^T$ :

$$\Psi_{\cdot,a}^{(s)} = Ue^{-s\Lambda}U^T\delta_a \implies \forall m, \quad \Psi_{m,a}^{(s)} = \delta_m^T Ue^{-s\Lambda}U^T\delta_a = \sum_{j=0}^{N-1} e^{-s\lambda_j} U_{aj}U_{mj}$$

where  $\delta_m$  is the indicator vector associated to node  $m$ , and  $e^{-s\Lambda}$  is the diagonal matrix  $\text{Diag}(e^{-s\lambda_0}, e^{-s\lambda_1}, \dots, e^{-s\lambda_{N-1}})$ .

In order to compute these wavelets in a tractable fashion that extends to large graphs, Hammond and al [13] suggest the use of Chebychev polynomial approximations. In this setting, the authors use the fact that a continuous function on the compact set  $[0, \lambda_{\max}]$  can be uniformly approximated by a polynomial as:  $e^{-\lambda s} = \sum_{k=0}^K \alpha_k \lambda^k + r(\lambda)$ , where  $|r(\lambda)| < \epsilon$ ,  $\forall \lambda \in [0, \lambda_{\max}]$ ,

and the  $\alpha_k$  are the coefficients of the polynomial approximation. The wavelets are then simply given by:

$$\begin{aligned}
 \Psi_{\cdot,a}^{(s)} &= U[P(\Lambda) + r(\Lambda)]U^T \delta_a = \sum_{k=0}^K \alpha_k U \Lambda^k U^T \delta_a + U r(\Lambda) U^T \delta_a \\
 \text{(D7)} \quad &= \sum_{k=0}^K \alpha_k L^k \delta_a + U r(\Lambda) U^T \delta_a
 \end{aligned}$$

where  $K$  denotes the order of the approximation. The cost of computing the wavelet transforms is simply  $O(K|\mathcal{E}|)$ —making spectral wavelets an attractive approach for characterizing structural roles.

It immediately follows from Eq. D7 that the heat wavelet coefficients can be related to the structural properties of the nodes (degree, number of open or closed triangles the node participates in, etc.)—weighted by the coefficients  $\alpha_k$ . Starting from this observation, in [8], the authors define a structural signature for each node as the unordered set of coefficients:

$$\text{(D8)} \quad \chi_a = \{\Psi_{m,a}^{(s)}\}.$$

By comparing these sets (or equivalently, these distributions), one captures information on the connectedness and centrality of each node within the network. Hence, these wavelet coefficients contain all the necessary information to characterize nodes' topological status within the graph.

390 SERRA MALL,  
 STANFORD, CA 94305, USA  
 E-MAIL: cdonnat@stanford.edu  
 susan@stat.stanford.edu